



# Effect of Loading Rate on the Progressive Damage and Crack Classification of Granite Based on Acoustic Emission Technique

P. K. Gautam<sup>1,2</sup> · Rishabh Dwivedi<sup>3</sup>

Received: 7 November 2022 / Accepted: 18 July 2023 / Published online: 31 July 2023  
© King Fahd University of Petroleum & Minerals 2023

## Abstract

In this study, we investigated the strength, deformation, failure, and acoustic emission (AE) characteristics of granite during the five uniaxial incremental rates of (0.5, 1.0, 1.5, 2.0, and 2.5 kN/s) for cyclic loading and unloading. It is found that the phase difference between the stress–strain and loading/unloading rate is dependent on the stress–strain hysteresis. A steady rise in the elastic moduli during unloading, a characteristic of strain hardening behavior, is seen. The AE signal can be divided into four phases: quiet, transition, active, and rapid AE development phases. It is observed that the Kaiser effect is more pronounced for the first and second cycles when the cyclic loading is below 1.5 kN/s. This directly reflects that the crack damage threshold rises with cycle number, and the loading rate decreases and remains constant. On the other hand, the Felicity effect is more significant for the second and third cycles during the above 2.0 kN/s cyclic loading. The Felicity ratio (FR) drops with increasing cycle count and loading rate. Hence, FR variation can also be classified into four phases during rock deformation and failure: Phase I,  $FR \geq 1$ ; Phase II,  $0.85 < FR < 1$ ; Phase III,  $0.6 < FR \leq 0.85$ ; and Phase IV,  $FR < 0.6$ . The results show how mechanical damage changes over time and how the cyclic loading paths are set up to affect the Kaiser and Felicity effects.

**Keywords** Granite · Acoustic emission · Cyclic loading · Hysteresis loop · Kaiser effect · Felicity ratio

## 1 Introduction

Rock is an engineering material that has parts of engineering geology, petroleum engineering, mining, and civil engineering that all require a deep understanding of how the mechanical properties of rock work in a complex state of loading and unloading stress conditions. When rocks are loaded and unloaded under such confined and unconfined stress conditions, the rock deformation and failure characteristics are very different. Throughout the cycle of loading–unloading in the rock, the primary microcracks

repeatedly close, reopen, and expand. The microcracks generally close because of applied stress when the cycle is in loading condition. In contrast, during unloading conditions, the existing cracks widen, or new ones develop. Because of this, the rock is less able to resist deformation, more deformation will happen, the rock's strength will decrease, and the stability of the rock structure will be at risk [1–6]. Therefore, rock engineers from all over the world have been looking into the rock's mechanical characteristics under cyclic loading and unloading conditions as a sign of long-term stability.

However, the acoustic emission (AE) technique has been successfully used recently to solve various problems in rock mechanics. AE characteristics can be used to monitor the progression of mechanical damage to rock materials caused by deformation and failure. AE is a transient stress wave induced by the sudden release of elastic energy within a material. It is preferable to other nondestructive techniques because it enables real-time monitoring of the evolution of deformation and the failure mechanism of rock samples. The AE technology should therefore be a “passive” nondestructive technique because it often only detects flaws as they emerge during the test [7–10]. AE technology is frequently

✉ P. K. Gautam  
pgautam.embedded@gmail.com

<sup>1</sup> State Key Laboratory of Geohazard Prevention and Geoenvironment Protection, Chengdu University of Technology, Chengdu, China

<sup>2</sup> Civil and Environmental Engineering, Colorado School of Mines, Golden, CO 80401, USA

<sup>3</sup> Department of Earth Sciences, Indian Institute of Technology, Bombay, India



used to identify a failure at an initial stage of damage, long before a structure entirely ruptures. The AE signature in rocks subjected to recurrent loading has a unique characteristic in which the AE produced is either zero or quite close to the background when the recurrent load is kept below the previously applied maximum stress. The AEs drastically increase as the stress level surpasses the prior maximum. This is referred to as the Kaiser effect. The Kaiser effect was first observed in metals (examined under tension) [11], and it was then verified in rocks (examined under compression) by [12]. The mechanism of this technique may store the most recent stress memory instead of the earlier applied maximal stress. Consequently, the Kaiser effect reflects the stressful memory of rocks about their loading history [13–16]. The Kaiser effect has the benefit of not mandating the usage of any deformation properties or disposal strain gauges. The Kaiser effect is an accurate estimation technique that may be used in the design and regular operation of engineering structure projects. After decades of experimentation, this technique of geotechnical-based stress measurements at laboratory scales is progressively gaining confidence in the discipline of rock mechanics and rock engineering. This technique has already been used commercially in Australia. The deformation and failure behavior of brittle rock materials was examined by [17]. Rao and Ramana [18] have used the applied acoustic emission (AE) and ultrasonic techniques to assess granite's uniaxial cyclic loading-induced gradual failure. Cox and Meredith [19] examined AE events that occur when rocks are softened and microcracked. Lockner [20] investigated the effects of the AE technique on the exploration of rock failure mechanisms. Li and Nordlund [21, 22] found that the effects of rock characteristics, stress levels, and paths revealed that not all rock masses exhibit the Kaiser effect. Pestman and Munster [23] investigated the link between AE characteristics and failure mechanisms, along with the stress memory of sandstone subjected to triaxial stress. Dai and Labuz [24] proposed AE for real-time concrete and rock damage prediction. Akesson et al. [25] studied the characteristics of crack initiation and propagation of anisotropic granite under uniaxial cyclic loading. Tham et al. [26] used a multichannel AE system to monitor the AE characteristics of stretching plate rock materials. They also used finite element software to do a simulated analysis of deformation and failure characteristics based on AE data. Ganne et al. [27] used AE technology to study brittle failure before rock peaks and classified the four stages of cumulative rock AE activity: initial, stable, active, and intense. Ishida et al. [28] conducted a study based on the AE techniques on the beginning of cracks in the rock in the course of straight shearing and observed that AE could be used to analyze data with great accuracy. How cracks developed when rocks were treated to a straight shearing test. Spasova et al. [29] used the AE monitoring approach to investigate the softening characteristics of rocks. Yang et al.

[30] observed the behavior of red sandstone under triaxial compression, examining how confining pressure and loading direction affected the rock's strength parameters, deformability, failure behavior, and AE locations. Zhao et al. [31, 32] used the AE technique under triaxial unloading to investigate granite damage and dilatancy characteristics from a high-level radioactive waste geological disposal deposit. Momeni et al. [33] employed four different frequencies (0.1, 0.2, 1, and 5 Hz) to assess the fatigue behavior of rocks at various maximum loads, frequencies, and compression amplitudes to determine how rocks are damaged by fatigue and the effect of the loading frequency on fatigue behavior during uniaxial cyclic compression. Fu et al. [34] examined the Kaiser effect of marble in the Brazilian tensile splitting test along with the three-point bending test to establish a link between the stress, strain, and AE data. Meng et al. [35] examined how strain rate and size affected the AE response of six separate rock specimens, each of six distinct sizes, to six varied strain rates subjected to uniaxial compression. Ranjith et al. [36] investigated critical stress by performing uniaxial loading experiments on cracked rock specimens using AE data. The AE count curve was used to identify three common stages: crack closure and linear elastic deformation, stable crack propagation and unstable crack propagation, and two major stress types: crack initiation and crack damage stress. Liu et al. [37] observed the mechanical and hydraulic properties of muddy sandstone specimens during triaxial compression. Their experiment revealed the failure mechanism using AE counts, and the alteration in permeability matched the AE amplitude. Wu et al. [38] observed an AE monitoring technique to examine the deformation and failure mechanism of cracked sandstone specimens. They examined the relationship between the AE count and the cracking process in sandstone specimens with pre-existing cracks of varying lengths. Huang et al. [39] used brine-saturated sandstone specimens in several triaxial compression tests with varying confining stress. During the deformation process, ultrasonic velocity and real-time AE were examined, demonstrating the four stages of development of the AE count and primary wave (P-wave) velocity.

Several studies have been conducted on rock strength parameters, deformation, failure, and AE characteristics under uniaxial compression, triaxial compression, tension, shearing, and monotonic loading [40]. However, it is commonly seen that rock deformation and failure in engineering disciplines are complicated under cyclic loading–unloading conditions. Hence, the study of time-dependent mechanical damage in rock materials under cyclic loading based on the AE technique is essential. Using the AE technique, cyclic compression loading tests reveal extremely intricate mechanical characteristics of rock materials than uniaxial and triaxial compression testing. It is necessary to perform more research on the rock AE characteristics caused by diverse applied

stress and various rates of loading–unloading cycles. The b-value of AE has been investigated extensively to reflect the growth and modification of microcracks during rock fracture. The most widely used approach for investigating fracture modes during rock loading is the JCMS crack distribution classification [41]. This approach is used to calculate the two AE characteristics, the rising time of maximum amplitude (RA) and average frequency (AF), which are utilized to differentiate between tension and shear crack types [6, 42]. Therefore, the evaluating the macroscopic failure features, it is possible to compare and investigate the onset and growth of fracture processes in rock mechanics under different stress conditions using the b-value and RA–AF distribution.

Therefore, the primary objective of this research work is to comprehend how granite is progressively damaged and crack classification distribution over time based on strength, deformation, and AE characteristics under uniaxial cyclic loading and unloading at the constant stress lower limit.

## 2 Experimental Procedure and Methods

### 2.1 Granite Preparation

The investigated granitic rock samples were obtained from surface outcrops in Sichuan Province, China. It is a relatively fine-grained ( $\approx 1$  mm) granite with a gray color. Albite, quartz, biotite, and microplagioclase are the primary mineral compositions. The granite was cored to have twenty cylindrical specimens, each measuring 50 mm in diameter and 100 mm in length, as shown in Fig. 1a. The specimen's end was parallel ground on a surface roughness deviation of less than 0.03 mm. Table 1 summarizes the average physico-mechanical properties of intact granite rock samples.

### 2.2 Experimental Techniques

#### 2.2.1 MTS 816 Setup

A servo-controlled testing MTS 816 system was used to conduct the uniaxial compressive strength (UCS) tests at SKLGP, Chengdu University of Technology, China. The system's maximum load capacity is 4600 kN. (Accuracy of 0.01 kN). Closed-loop control of servo-hydraulic tests is conducted employing both hardware and software components. The cyclic testing machine is made up of a compressive loading frame, an axial cyclic loading system, and a data acquisition (DAQ) unit. Signal conditioning and an acquisition device connected to a computer make up the data acquisition system. Data are recorded on all channels using

multiple or single data collection methods. The machine has an automatic dynamic control mode that allows it to switch between connected transducers. The servo sensitivity was 290.0 Hz (with a 0.1 Hz accuracy), and the sampling frequency was 5.0 kHz. A 6-mm range linear variable differential transformer (LVDT) was installed to determine the axial displacement. This research used five uniaxial cyclic loading–unloading compression techniques with five varied loading rates (0.5, 1.0, 1.5, 2.0, 2.5 kN/s), as shown in Fig. 1b and Table 2. Four rock specimens were tested for each loading rate. In each step of the cyclic loading process, the load was only reduced by 1 kN. This was done so the specimen wouldn't slide off the compression head. During the cyclic tests, each specimen was loaded four times continuously from 0kN  $\rightarrow$  to 20.0kN  $\rightarrow$  1 kN  $\rightarrow$  to 60.0 kN  $\rightarrow$  1 kN  $\rightarrow$  to 100.0 kN  $\rightarrow$  1kN  $\rightarrow$  to 130kN  $\rightarrow$  1kN with a force-controlled mode applied. But, after the fifth loading, a monotonic uniaxial compression with a displacement-controlled base (loading rate = 0.2 mm/min) was used until the granite rock specimens rupture failure occurred.

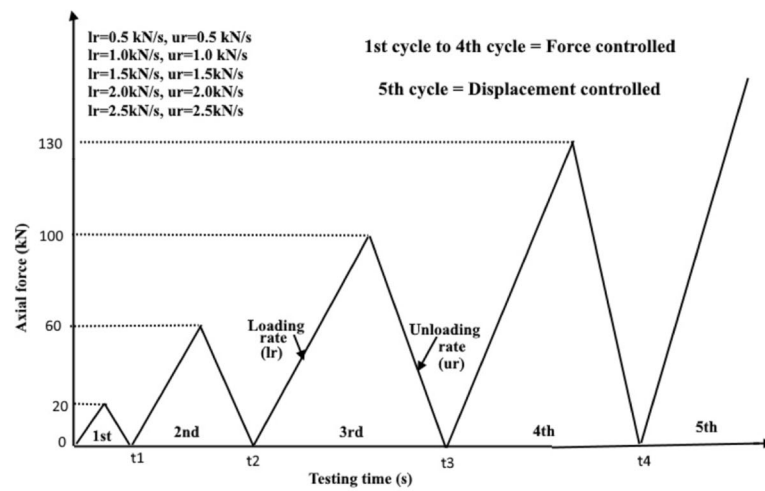
#### 2.2.2 AE Setup

Six Nano 30 AE sensors were circumferentially mounted on the cylindrical and top-to-bottom surfaces of granite rock specimens to measure the arrival time, amplitude, and vibration of the AE signatures from each sensor, as shown in Fig. 1c. To ensure that the ceramic end of the AE sensor and the rock specimen surface make better contact, the ceramic end is coated with a coupling substance and the electrical tape is tightly pasted to the rock specimens to mitigate end of friction. However, AE data logger settings were confirmed, and the AE monitoring system was calibrated repeatedly by breaking a pencil tip at the rock specimen's midpoint until a reliable and consistent AE count was achieved. Although the sensor's operating frequency range was 125–750 kHz, its resonant frequency was 300 kHz. The AE sensors were configured to a sampling rate of 1 MHz to record the acoustic energy produced by the granite rock specimens during cyclic compression. These recorded AE signatures were converted to electrical signals and then amplified 40 dB by a pre-amplifier. All transducers were connected to MISTRAS 2/4/6 pre-amplifiers coupled with a 20 kHz to 1 MHz frequency filtration system. The PCI-2 AE system was used to acquire all AE and time history data in real time at a 40 dB threshold and a 5 MHz sampling rate. The signals from the transducers are amplified and supplied into the data acquisition PCI-2 AE system, which schematically depicts a signal processing-based continuous digital monitoring system, as shown in Fig. 1d.

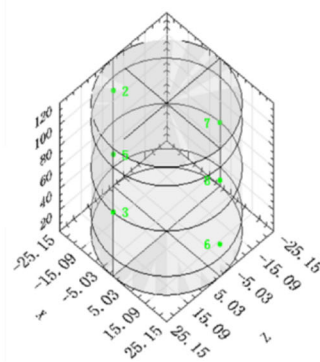
**Fig. 1** **a** Granite rock specimens in uniaxial cyclic loading and unloading tests. **b** Schematic diagram of the loading–unloading stress path. **c** Schematic diagram showing the locations of the AE sensors mounting layout for rock specimens. **d** Loading–unloading compression and acquisition system schematic and an acquired signal are fed through an array of pre-amplifiers ( $\times 40$  dB) and fed in parallel to the trigger-based and continuous monitoring systems



(a)



(b)



Sensor coordinates,mm			
Sensor channel	X	Y	Z
2	-25.000	90.000	0.000
3	0.000	60.000	25.000
5	-25.000	30.000	0.000
6	25.000	30.000	0.000
7	0.000	60.000	-25.000
8	25.000	90.000	0.000

(c)

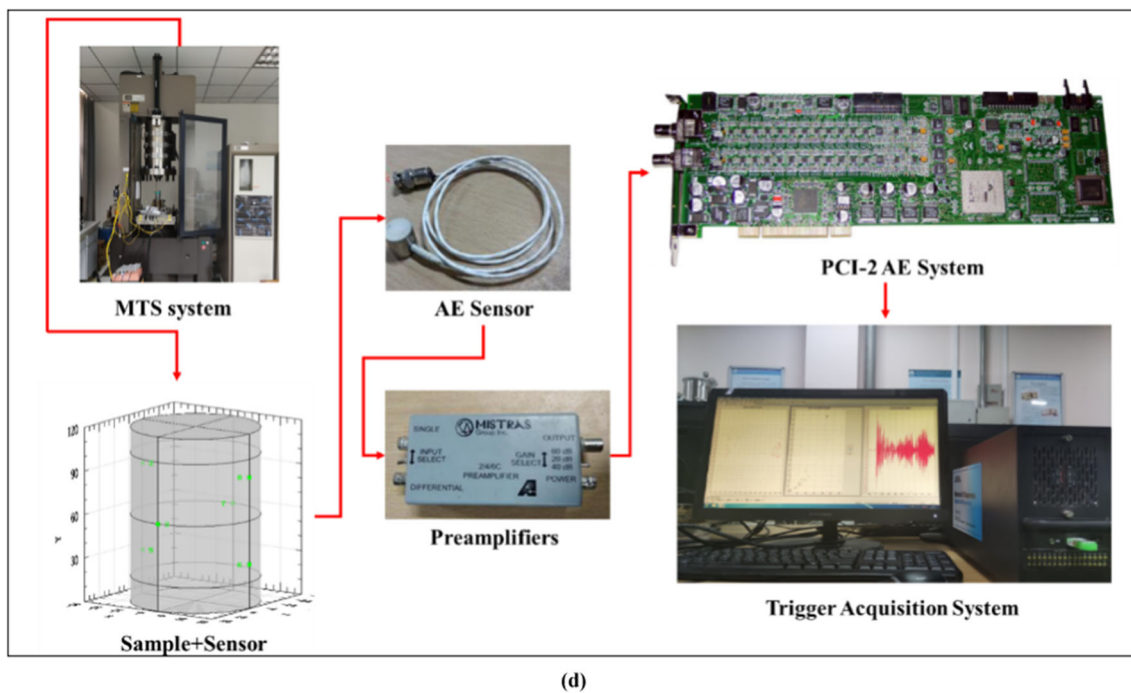


Fig. 1 continued

**Table 1** Physical and mechanical properties of the intact granite rock sample

Density (g/cc)	UCS (MPa)	Elastic modulus (GPa)	Poisson's ratio	P-wave velocity (m/s)
2.641	92.86	14.66	0.29	6941

**Table 2** Scheme of the granite uniaxial cyclic loading–unloading experiment

Rock specimens	Loading rate (kN/s)	Unloading rate (kN/s)
1#, 2#, 3#, 4#	0.5	0.5
5#, 6#, 7#, 8#	1.0	1.0
9#, 10#, 11#, 12#	1.5	1.5
13#, 14#, 15#, 16#	2.0	2.0
17#, 18#, 19#, 20#	2.5	2.5

### 3 Results

#### 3.1 Variation of the Stress–Strain Curve

The stress–strain curves of granite rock specimens were drawn during direct uniaxial compression testing with a loading rate of 0.2 mm/min. In the initial loading stage, the curve had a convex shape, indicating that crack initiation had not occurred. As the stress increased, the slope of the curve gradually increased until, eventually, the specimen attained the yielding stage. It can be inferred that after getting the peak value, there was a noticeable drop in stress,

which is most likely caused by internal damage to the rock structure. The comprehensive stress–strain curves of granite rock specimens under uniaxial cyclic loading–unloading compression at varied loading rates are illustrated in Fig. 2a, b, c, d, and e. However, the stress–strain curves show similar patterns during different uniaxial cyclic loading–unloading rates. We found that the granite specimen's average uniaxial peak compressive strength during monotonic compression was 92.86 MPa, while the average compressive strength was 86.88, 96.04, 90.09, 100.05, and 69.30 MPa under various cyclic uniaxial loading–unloading rates off 0.5, 1.0, 1.5, 2.0, and 2.5 kN/s, respectively. Compared to direct loading peak stress, the cyclic loading peak stress for 1.0 and 2.0 kN/s is higher by 3.42 and 8.2%, respectively. In contrast, cyclic loading peak stress decreases by 6.4, 3.42, and 25.3% compared to direct loading peak stress for 0.5, 1.5, and 2.5 kN/s, respectively. The elastic deformation increased as the number of cycles increased, and the loading and unloading curves started to deviate to the right. It is found in the first cycle (0.0 kN → to 20kN → 1 kN) and second cycle (1 kN → to 60kN → 1kN), the stress–strain curve gradually intensified, and consequently, the granite moved into the steady deformation stage. Hence, the granite slowly compacted, and it would be anticipated that the stiffness should rise. Additionally, the

unloading and the loading curve progressively converged. In the hysteresis loop, the curve joins the original curve rather than returning to its origin during the subsequent loading process. We found that the hysteresis loops were higher during the third cycle (1 kN → to 100kN → 1kN) and the fourth cycle (1 kN → to 130kN → 1 kN). Subsequently, when the strain recovers during the unloading stage, the hysteresis loop may not be completely closed, probably caused by intergranular viscosity and friction between the microfractures. The enveloped regions of the hysteresis loops in the stress–strain curves represent the dissipated energy [43–45]. The hysteresis loops in enclosed areas increase, indicating that more energy is needed to break down the specimen's structural integrity [46]. However, various loading–unloading cycles vary due to different degrees of damage to rock materials. The loading, unloading, and reloading curves may all be subdivided into approximately linear segments and other regions. Four cyclic reloading curves are investigated, as shown in Fig. 3. These reloading stress curves show a consistent evolving pattern and a high overlap ratio as they change at different stress level rates [30, 47, 48]. The reloading curve starts at the point where the earlier unloading curve ended, and it follows a straight line. This caused the reloading stress of different cycles to shift and seem nearly paralleled because the degree of rock material damage varies based on the number of cycles and stress level rate. The reloading curves become more nonlinear and steeper as the load-unloading cycle rate rises. When applied stress was more significant than the previous maximum stress (PMS), the gradient of strain dependency on stress changed slightly, and this change happened due to the stress memory effect [49–52].

### 3.2 Time-Dependent Stress–Strain Characteristics and Failure Morphology

The time-dependent stress–strain characteristics are a function of real-time-based stress–strain memory as shown in Fig. 4. However, increasing the loading rate, the strain rate of rock specimens is also increased. The strain rate is an index that measures the rate of change in deformation and fractures of rock, which also reflects the change rate of stress level. It is found that the strain rate of the rock specimen is about  $6.54 \times 10^{-6} \text{ s}^{-1}$ ,  $1.18 \times 10^{-5} \text{ s}^{-1}$ ,  $1.58 \times 10^{-5} \text{ s}^{-1}$ ,  $1.84 \times 10^{-5} \text{ s}^{-1}$ , and  $2.35 \times 10^{-5} \text{ s}^{-1}$  under different cyclic loading–unloading rate of 0.5, 1.0, 1.5, 2.0, and 2.5kN/s, respectively. It is observed that the strain hardening phenomena are related to a lower strain rate at 0.5kN/s and 1.0kN/s. In contrast, the strain-softening phenomena were found with increasing unloading cycle numbers at 1.5kN/s, 2.0kN/s, and 2.5kN/s. After the fourth cycle, the compressive strength of the rock specimens was 14.11, 14.21, 17.70, 14.81, and 11.53 MPa, respectively. At a high strain rate, a large amount of energy in a very short time induces existing cracks to develop along the

shortest paths to higher resistance. The reason may be due to the breakage of the rock in crack damage failure, and the accumulated damage weakened the specimen before breakage. However, the average strain energy rate can demonstrate the rate of change of the whole failure mechanism of rock. However, the maximum strain rate shows the rock's mechanical characteristics when the most significant deformation change occurs. Hence, the accuracy of stress determination depends on the material strength composed of frictional strength, where friction is reduced to cohesion and accounts for the time-dependent behavior of the interface of the sliding planes [53]. It is revealed that under controlled stress ranges, the strain rate substantially affects the failure morphology of specimens, as shown in Fig. 5. On the other hand, the primary fracture planes are roughly parallel to axial splitting and shear faulting directions. Shear failure, tensile failure (also referred to as splitting failure), and mixed tensile-shear failure are the most common types. One or more oblique fracture planes can lead to shear failure, while tensile failure occurs when a rock failure is on a vertical fracture plane. Tensile failure was observed to form long slabs along the edges of specimens at loading–unloading cycles between 0.5 and 1.0 kN/s. In contrast, in the loading–unloading cycles with 1.5, 2.0, and 2.5 kN/s, there was a small shear failure at the edges and a large tensile failure along the failure plane. It is noteworthy that, at 2.5 kN/s, a well-developed shear plane causes the rock sample to split and cone-shaped fragments to occur. Hence, each granite sample exhibits both shear and tensile failure at low loading–unloading rates (0.5 to 1.5 kN/s), and a single well-developed shear failure plane is observed with increasing loading–unloading rates above 2.0 kN/s. After the specimen failed, there were 2–3 rock blocks with fewer broken blocks. The failure plane angle of the granite rock specimens is discovered to, 85.3, 83.1, 81.2, and 79.9° under the cyclic loading–unloading rate of 0.5, 1.0, 1.5, 2.0, and 2.5kN/s, respectively. The failure plane angle of the rock decreases as the uniaxially cyclic loading–unloading stage increases. It indicates that when the rate of cyclic compression of specimens increases, the failure mechanism of the rock sample progresses from shear failure to tensile failure, and the failure degree enhances. Therefore, the main failure mechanism of granite specimens changes from tensile to mixed tensile shear to tensile [54, 55].

### 3.3 Variation of Cyclic Elastic Modulus

The corresponding elastic modulus under the various cyclic loading–unloading compression is determined as depicted in Fig. 6. This indicates that under the unloading path, the rock elastic modulus is enhanced to some extent. The change in the specimens' elastic modulus is calculated using the stress-to-strain ratio on the stress–strain curve at half the peak stress. Due to the repetitive loading–unloading of the specimen,

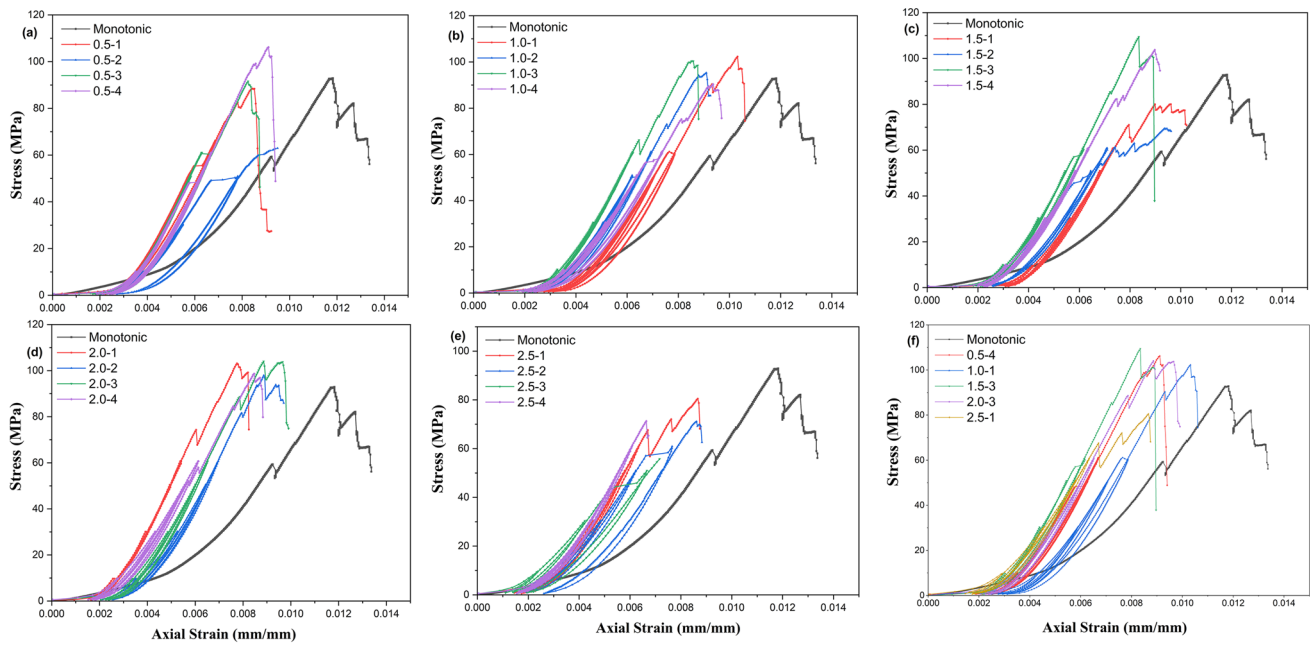


**Fig. 2** Complete stress–strain curves of rock specimens during uniaxial cyclic loading and unloading compression with different loading rates. **a** 0.5kN/s, **b** 1.0kN/s, **c** 1.5 kN/s, **d** 2.0kN/s, **e** 2.5 kN/s, and **f** comprehensive stress–strain curve

each loading–unloading cycle may produce a loading and an unloading elastic modulus.  $E_0$  stands for the elastic modulus acquired in the first loading–unloading cycle,  $E_1$  for the second loading–unloading cycle, and so forth until  $E_n$ , which stands for the  $n$ th loading–unloading cycle. Equation 1 is used in Table 3 to estimate the specimens’ elastic moduli during the cyclic loading–unloading process [56, 57].

$$E_0 = \frac{\sigma_{1mid} - \sigma_{1min}}{\varepsilon_{1mid} - \varepsilon_{1min}} \tag{1}$$

Here,  $\sigma_{1mid} = \frac{\sigma_{1max} + \sigma_{1min}}{2}$  &  $\varepsilon_{1mid} = \frac{\varepsilon_{1max} + \varepsilon_{1min}}{2}$ .

$E_0$  is the elastic modulus,  $\sigma_{1mid}$  is the half of the maximum axial stress in each cycle,  $\sigma_{1min}$  is the minimum axial stress in each cycle,  $\varepsilon_{1mid}$  is the axial strain corresponding to  $\sigma_{1mid}$ , and  $\varepsilon_{1min}$  is the axial strain corresponding to  $\sigma_{1min}$ .

The stress at the unloading point must be lower than the point at which the intersections with the loading curve for an elastic limit. Thus, the irreversible deformation that takes place is different from that of the initial unloading curve. This demonstrates that irreversible deformation causes a slight increase in rock elasticity during the unloading stages. It indicated that the elastic modulus progressively increases in the unloading stages than in the reloading stages. When the loading rate is 0.5kN/s, with increasing the number of cycles, the elastic modulus of granite first rises and then tends to be stable. The elastic modulus, however, is significantly higher during the unloading stage than during the loading stage. When the loading rate is 1.5 and 2.0kN/s and the number of

cycles rises, the elastic modulus of granite increases significantly. Enhanced cyclic loading rate has a significant impact on strengthening granite’s elastic modulus. As the number of cycles increases and the loading rate is 2.5 kN/s, the elastic modulus of granite marginally increases. The reason is that the specimen’s internal cracks are closed by extrusion and then sustained in an equilibrium state because of the high loading rate (2.5 kN/s). In this scenario, elastic energy is predominant, which is retained by the specimen. The comprehensive stress–strain curve under different uniaxial cyclic loading–unloading rates has a concave shape and hysteresis loops, which vary from loose to dense along with deformation, as shown in Fig. 2f. During the reloading process, the curve does not follow its original path but rather gradually overlaps it to form a hysteresis loop. The dissipated energy defines the hysteresis loop area from the crack closure, crack initiation, crack coalescence, and crack propagation of the loaded rock sample until failure. If the hysteresis loop area were more significant, the rock sample would be severely damaged due to increased dissipation energy. As the number of loading–unloading cycles and stress levels rises, the hysteresis loop shifts toward the direction of strain growth. The comparison study shows that the fourth cycle had a more significant proportion of open hysteresis loops. The reloading curve is nearly straight when drawn from the prior unloading curve’s endpoint. The progression of these reloading stress profiles at varied stress levels maintains an identical shifting pattern with a high overlapping ratio. This result shows the relative increases in strain during the loading stage when the

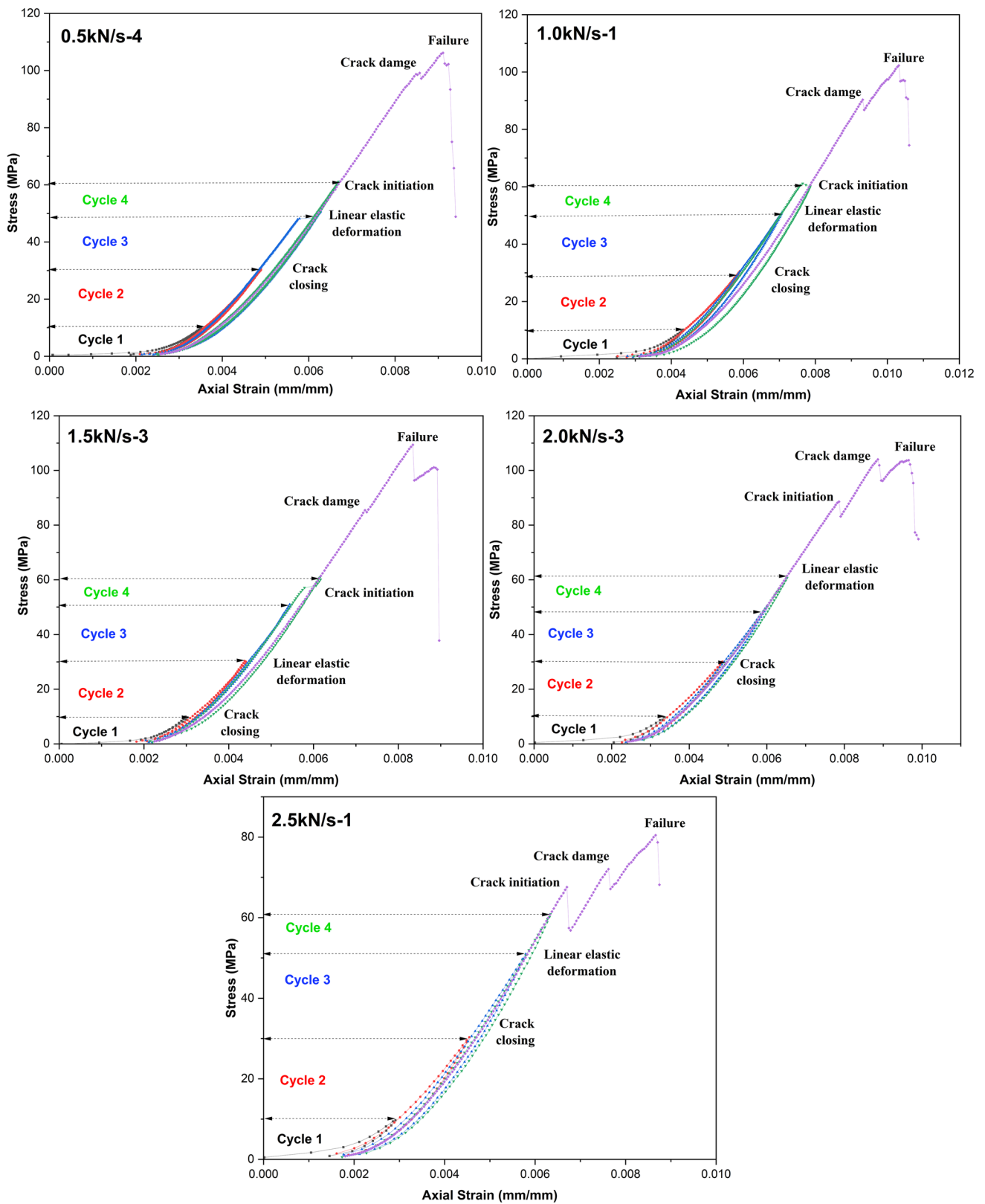


Fig. 3 Variation of cyclic reloading pattern of granites



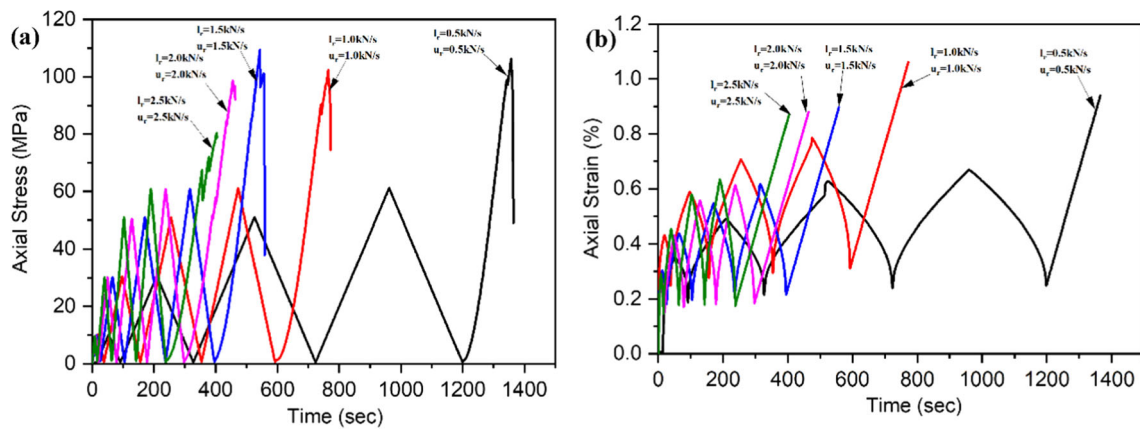


Fig. 4 Variation of loading path from a uniaxial cyclic loading and unloading a stress path and b strain path

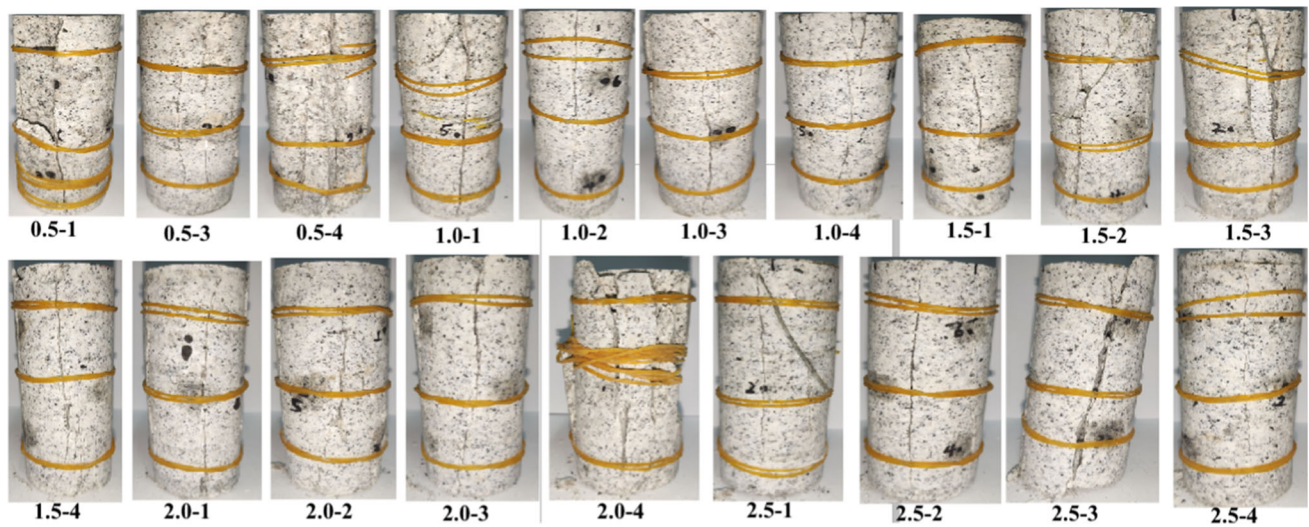


Fig. 5 Failure morphology of granite rock specimens after uniaxial cyclic loading and unloading

loading and unloading rates are similar. Hence, considering all specimen curves into perspective, hysteresis loops of specimens at a 0.5 kN/s loading rate were loose, while hysteresis loops of specimens at a 2.5 kN/s loading rate were denser. It shows irreversible deformation due to cyclic loads rising with the cyclic loading rate. Therefore, rock grain particles' resistance to squeezing deformation improves when the load rate rises. Thus, the strain rate progressively increases when the rock material is deformed again by the loading effect (at the reloading stages). Consequently, experimental investigation of irreversible deformation and fracture development revealed that cyclic loading affects specimens in two distinct ways: (1) The improvement and stability of strength and elastic modulus at loading–unloading rates less than 1.5kN/s, and (2) as the cycle of loading stages increased above 2.0kN/s, it indicates an increase in internal fracture and deformation, as well as an increase in the degree of failure angle of rock material with time. Hence, the degree of damage to the rock material highly depends on the number of cycles.

This results in a variation in the reloading stress across different cycles that seem roughly parallel and nonlinear and steeper reloading curves as more loading–unloading cycles are performed. The loaded rock specimen's failure mode is an essential attribute that reveals its deformation and failure mechanism. The rock specimen's failure mode under various uniaxial cyclic loading–unloading is illustrated in Fig. 5. When the cyclic loading rates are below ( $\geq 1.5$ kN/s), axial splitting is the primary failure mode of the rock specimen (tensile cracking). When the cyclic loading is high ( $\geq 2.0$  kN/s), single conjugate tensile failure and shear crack failure modes dominate [58].

### 3.4 Evolution of AE Signatures

The granite specimens are under different states of variation curves, i.e., the axial strain, stress, accumulated energy, and amplitude versus time, as illustrated in Fig. 7. The evolution of the cumulated AE energy and AE amplitude is also

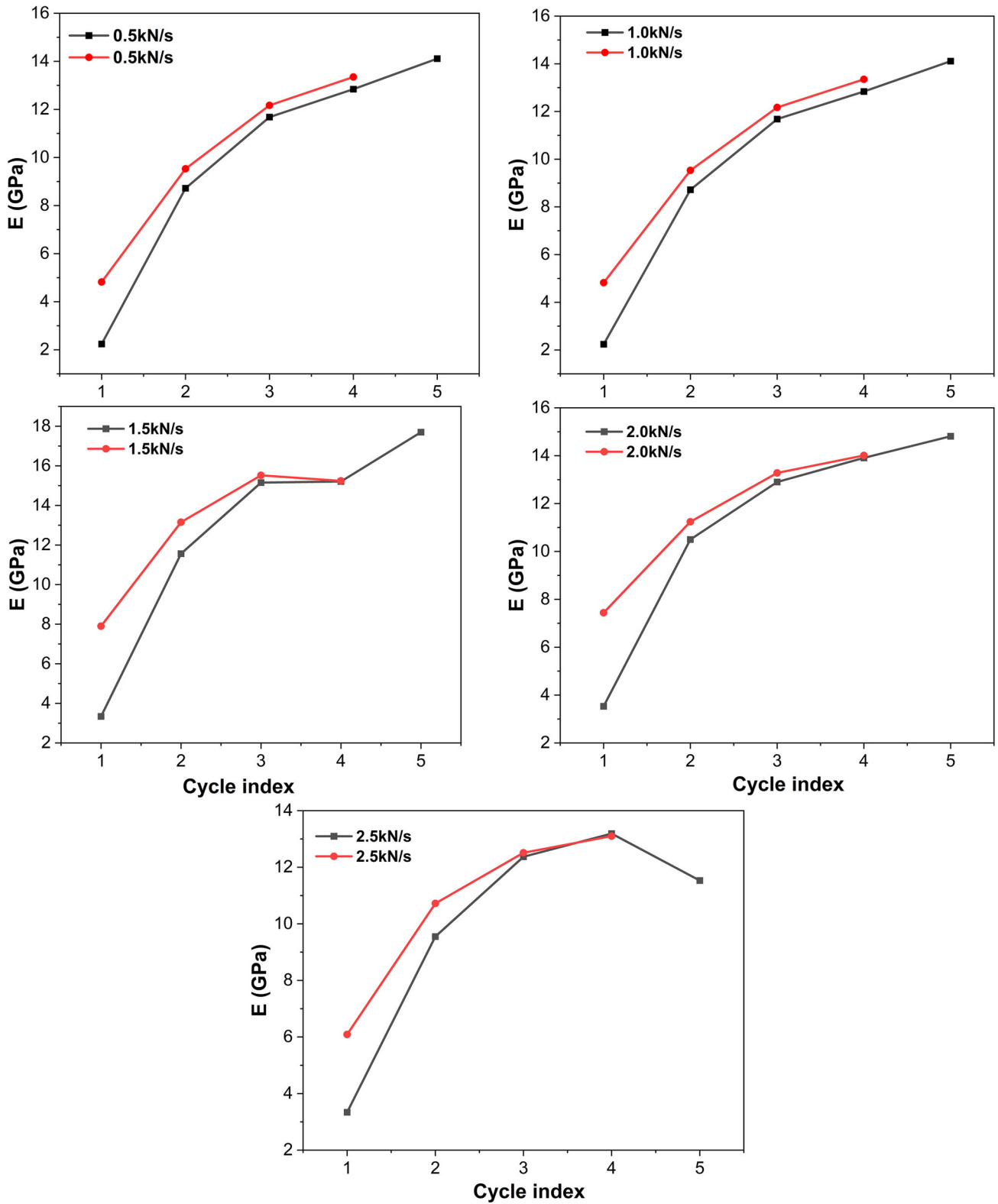
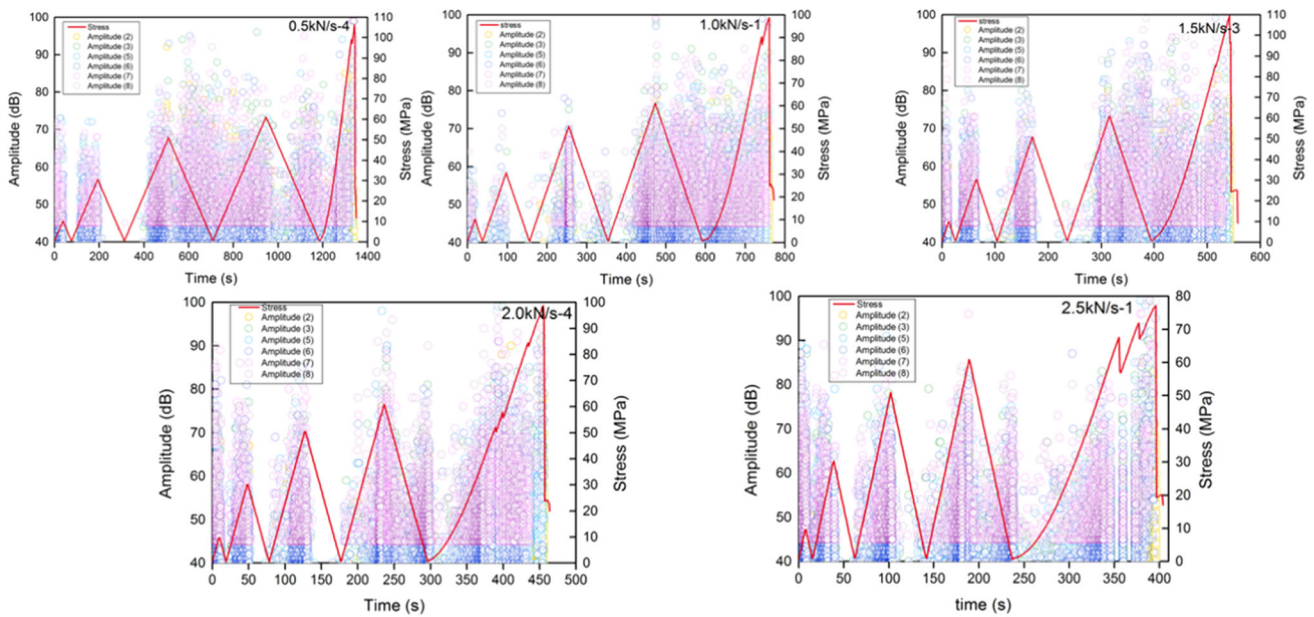


Fig. 6 Variation cyclic elastic modulus

**Table 3** Elastic modulus based on uniaxial cyclic loading–unloading compression

Elastic modulus (GPa)  $l_r$  = Loading rate;  $u_r$  = Unloading rate

Cycle index	0.5kN/s		1.0kN/s		1.5kN/s		2.0kN/s		2.5kN/s	
	$l_r$	$u_r$	$l_r$	$u_r$	$l_r$	$u_r$	$l_r$	$u_r$	$l_r$	$u_r$
1	2.24	4.82	2.24	4.82	3.34	7.90	3.53	7.44	3.34	6.09
2	8.72	9.53	8.72	9.53	11.56	13.15	10.50	11.24	9.55	10.72
3	11.68	12.17	11.68	12.17	15.15	15.52	12.90	13.28	12.37	12.51
4	12.84	13.35	12.84	13.35	15.21	15.24	13.91	14.01	13.19	13.10
5	14.11		14.11		17.70		14.81		11.53	



(a)

**Fig. 7** Variation of AE signatures: **a** amplitude and stress. **b** Cumulative AE energy and axial strain

strongly linked to the stress levels encountered along with the loading–unloading cycles and can be categorized into four stages: (1) compaction, (2) elastic stage, (3) crack initiation (both stable and unstable expansion stages of the cracks), and (4) peak-stress drop stage. Furthermore, the crack closure stage, elastic stage, dilatancy stage (growth of new fractures), and macroscopic failure stage are used to evaluate granite’s deformation and failure properties. Consequently, the AE evolution consists of a quiet phase, a transition phase, an active phase, and a rapid AE development phase. The conventional evolution of AE activity and the associated rock specimen failure mechanism can be fully explained as follows:

(1) The quiet phase ranges from 0 to 498, 0–485, 0–307, 0–229, and 0–98 s under cyclic loading–unloading rate

of 0.5, 1.0, 1.5, 2.0, and 2.5kN/s, respectively. This corresponds to the cyclic loading with the compaction stage of the stress–strain curve. Hence, a small amount of low cumulative AE energy and amplitude with noticeable fluctuations are observed in Fig. 7a and b.

(2) The elastic deformation phase compaction is represented by the transition periods of 498–703, 485–490, 307–393, 229–227, and 98–198 s during cyclic compression at 0.5, 1.0, 1.5, 2.0, and 2.5kN/s, respectively. In this phase, no damage was detected, and stress applied to the rock specimens is usually inadequate for new cracks. However, a small amount of cumulative low AE energy and amplitude is still produced when inevitable closed cracks open.

(3) The active phase period varies from 703–1198, 490–631, 393–501, 297–378, and 189–323 s under 0.5,

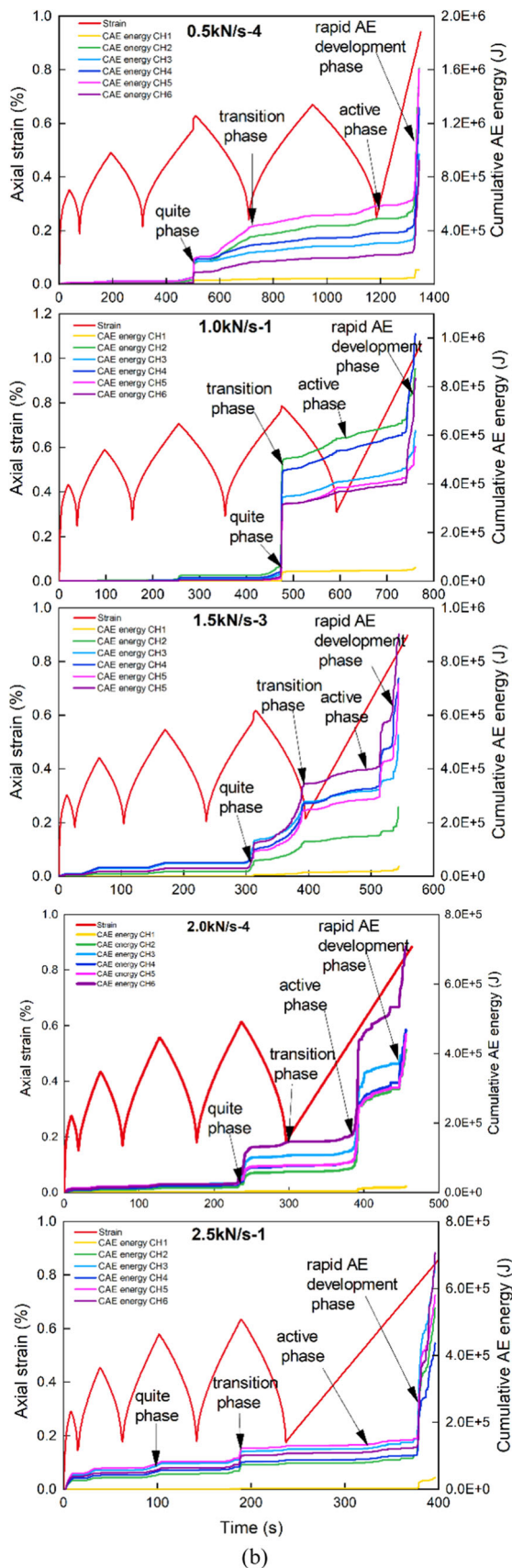


Fig. 7 continued

1.0, 1.5, 2.0, and 2.5kN/s, respectively, which corresponds to the crack initiation phase of the stress–strain curve. Microcracks in the rock sample are continuously generated and enlarged as the axial stress rises. However, the higher crack density will take longer to close, and more significant deformations will occur at this stage. With increasing cumulative AE energy and amplitude, the AE activity becomes effective. The AE signal's waveform was characterized by a dense high amplitude distribution, with rock spalling and expelled rock fragments as failure phenomena. The AE activity is highly active after collapse, with the dissipation of greatest amount of cumulative AE energy.

- (4) Deeply connected are the rapid AE development phase periods of 1198–1341, 631–753, 501–542, 378–464, and 323–403 s under 0.5, 1.0, 1.5, 2.0, and 2.5kN/s, respectively, which correlates to the macroscopic failure stage of the stress–strain curve owing to microcracks. The reason for this was that each cycle produced microcracks, which then connected and developed large fractures after the increased loading rates and stress levels. The cumulative AE energy curve, however, was around the peak stress, indicating significant damage at this point. Hence, the cumulative AE energy and amplitude both increased significantly in this phase.

### 3.5 Spatiotemporal Distribution of Cracks of AE Events

The change of stress, strain, duration, and AE events during varying rates of uniaxial cyclic loading–unloading are illustrated in Fig. 8. As the number of AE event points rises with the number of cycles and loading rates, the internal deterioration of the rock has worsened, causing the formation of fresh fractures. These rock damage impacts could be seen in different cyclic loading–unloading stages. The potential for crack development could be anticipated, as explained in detail below.

- (1) As illustrated in Fig. 8a and b, during the 0.5 and 1.0 kN/s cyclic loading–unloading condition, the granite rock specimen is in compaction in the first cycle from 0 kN → to 20.0 kN → 1 kN. The pre-existing microcracks and pores are closed to generate the AE locating points. The AE defect points are primarily in the center of the specimen when the stress in the second cycle goes from 1 kN → to 60.0 kN → 1 kN, which is influenced by the elastic stage. The AE defect points, as well as the center portion of the specimen, continue to increase; this is because the pre-existing microcracks and natural discontinuities are primarily closed in the center of the rock specimen. The AE defects points are

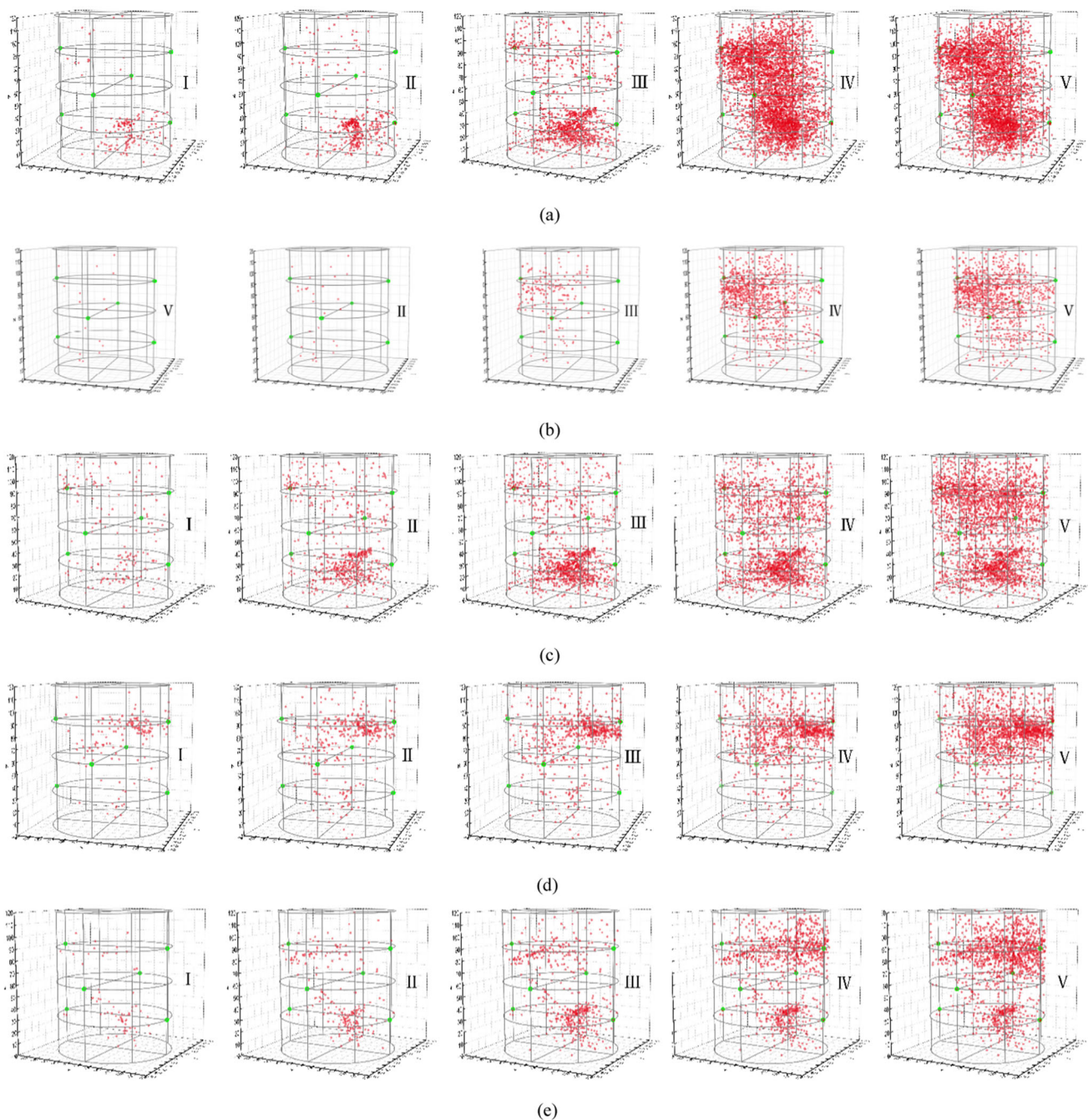


**Fig. 8** Spatial distribution diagrams of the AE for the granite rock specimens under uniaxial cyclic loading–unloading. **a** 0.5 kN/s. **b** 1.0 kN/s. **c** 1.5 kN/s. **d** 2.0kN/s. **e** 2.5 kN/s

developed diagonally to the top–bottom at the higher and lower parts of the prior AE defects points during the third cycle from 1kN → to 100.0kN → 1kN; this indicates that the specimen’s fracture grows in the diagonal direction from top to bottom. When the stress level reaches 1kN → to 130kN → 1kN in the fourth cycle, the AE defect points in the center of the specimen rise dramatically, and defects on the left and right initiate to

form through the center. The AE events achieve their maximum value, and new AE defect points develop on the specimen’s left, right, and center sides. Consequently, the specimen’s developed macroscopic failure at the final fracturing morphology indicates maximal AE events.

(2) The granite rock specimen is in the first cycle from 0 kN → to 20.0 kN → 1 kN, which is the compaction stage at

1.5 and 2.0 kN/s uniaxial cyclic loading–unloading rates as illustrated in Fig. 8c and d. The number of AE defect points mostly on specimens significantly rises and is spread randomly. The AE locating points are dispersed because of the microcracks. As soon as the stress level reaches the second cycle from 0 kN → to 60.0 kN → 1 kN, the stiffness of rock matrix rock specimens keeps rising, which is reflected by elastic deformation. The AE locating points in the center of the specimen rise significantly when the stress levels reach at third cycle from 1kN → to 100.0kN → 1kN; this is due to the wing fractures on the left and right started expanding through the center. The AE defects points are accumulated at the midpoint of rock specimens when the stress levels reach the fourth cycle from 1kN → to 130kN → 1 k, this is due to the cracks on the left and right wings propagating through, and the AE events attain their maximum. When the stress level approaches the maximum after the fourth cycle, the fractures have fully developed and have begun to create macrocracks. The corresponding number of AE defect points is at its maximum [59].

- (3) As illustrated in Fig. 8e, during 2.5 kN/s cyclic loading–unloading conditions, the granite rock specimen is underway in the first cycle’s compaction phase from 0 kN → to 20.0 kN → 1 kN. It is found that a few AE defect points developed in the center and lower inner portions of the intensive rear alignment of the left end faces took place at this stage of the specimen. The AE defect points of the left end surface continue to rise when the stress levels increase in the second cycle from 1 kN → to 60.0 kN → 1 kN. The AE location points on both sides of the specimen are significantly higher, suggesting that the cracks on either side develop simultaneously. The lower and center portions of the specimens’ AE defect points start to rise, and as soon as the stress level reaches the third cycle (from 1kN → to 100.0kN → 1kN), the cracks on the left and right start to converge and develop through the lower section. There is a concentration of locating points as the number of AE defect points rapidly rises, and the crack forms a nucleus when the stress level reaches the fourth cycle from 1kN → to 130kN → 1kN. Subsequently, the microcracks start to coalesce to form surface macrocracks, and a peak in AE events was observed. When the stress level exceeds the fourth cycle, the AE locating points emerge in dense regions, and the microcracks in the specimen start to develop.

### 3.6 Variation of b-Value

It is well known that the power law, which also applies to AE events in rocks, is being used in seismology by Gutenberg

and Richter [60] to formulate the relationship between the frequency magnitude spectrum of earthquakes as Eq. 2.

$$\log_{10} N(M) = a - bM \quad (2)$$

$N$  is the total number of earthquakes with a magnitude greater than  $M$ ,  $M$  is the earthquake’s amplitude on the Richter scale (which is a logarithmic scale), and  $a$  and  $b$  are constants. The  $b$ -value of the AE field is commonly used to assess the fracture process based on the principle that the mechanism of rock fracture is like that of an earthquake. As a result, the magnitude in the Gutenberg–Richter relationship is replaced by the amplitude when calculating the  $b$ -value represents the formula as Eq. 3.

$$\log_{10} N(A_{dB}) = a - b \frac{A_{dB}}{20} \quad (3)$$

where  $A_{dB}$  is the peak amplitude of AE events in decibels.

The variations of the  $b$ -value versus cycle index during uniaxial cyclic loading–unloading can be seen as depicted in Fig. 9. The  $b$ -value in AE is a measure of crack propagation and its variation with time. An increase in the  $b$ -value indicates an increase in the number of small AE events. In contrast, when the number of large AE events increases, the  $b$ -value decreases. The count of occurring AE events is stable when the  $b$ -value varies consistently and the range is small, which indicates that the growth of the fracture propagation is stable and progressive. Sometimes, the  $b$ -value fluctuates sharply, showing the rock is in an unstable accelerated fracture stage. But when the  $b$ -value rapidly decreases, the rock fails, and the fracture development has changed significantly.

It is observed that the  $b$ -value is initially relatively higher, and the fluctuation range is smaller under the cyclic loading–unloading rate of 0.5, 1.0 and 1.5kN/s, which shows the cracks developed in the interior of the rock are progressive and stable. There are a large number of small AE events, and the development of original and regenerated cracks of various shapes and sizes slows down. In contrast, the value is initially relatively smaller during the high cyclic loading–unloading rate of 2.0 and 2.5 kN/s, indicating a large number of major AE events. In terms of crack distribution, explaining how damage evolved from a largely random distribution to a preferred localization of the cracks toward the failure surface may be feasible.

Finally, the  $b$ -value is relatively higher under the loading rate below ( $\leq 1.50$ kN/s), indicating that a low loading rate restrains the cracks’ propagation and increases the rocks’ resilience to deformation. In contrast, the  $b$ -value is relatively smaller under the loading rate above ( $> 1.5$ kN/s); it may be due to the damage evolution of the rock in terms of crack distribution from the volume of random distribution

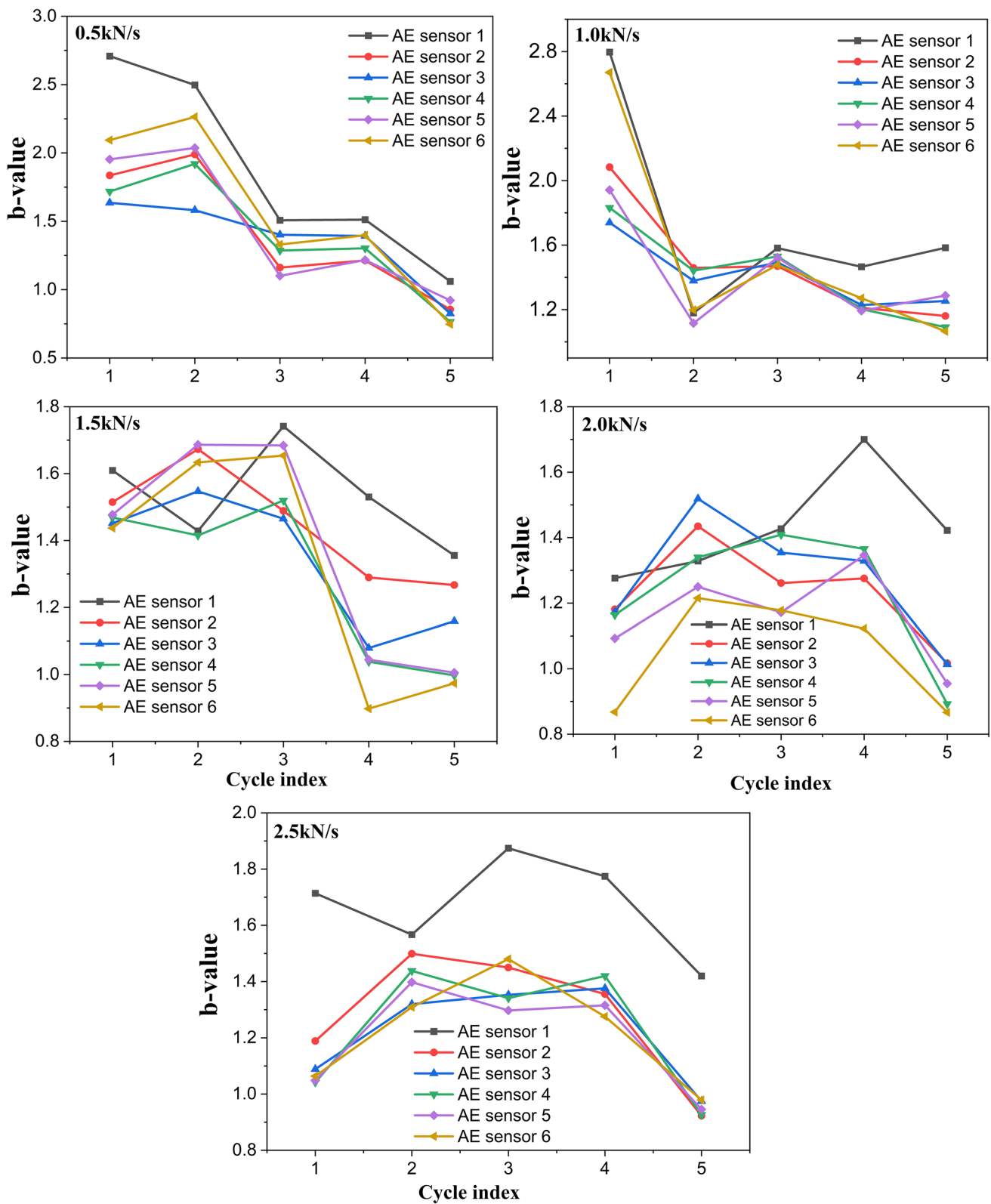


Fig. 9 Variations of b-value during different loading-unloading rates at different six AE sensors

to preferential localization of the cracks around the failure surface.

The rock steadily becomes more damaged as the number of cycles increases, and the strain hardening also increases. The cracks then begin to develop rapidly as the *b*-value starts to decrease. The fraction of large AE events increases, and it leads to generating many more larger cracks. Under the third cycle, the *b*-values slightly fluctuate, which clearly shows the unstable fracture stage of the rocks. This indicates that the sustained loading–unloading cycle exacerbates the structural damage to the rock, causing the cracks to coalesce rapidly into macrocracks. Finally, there is a very steep decline in the *b*-value. The abrupt change in the *b*-value is consistent with the rock's reduced stress. This indicates that the crack propagation accelerated inside the rock. As a result, in this stage of unstable accelerated fracture, the rock's macroscopic fracture surfaces have merged, leading to rock specimens' brittle failure.

### 3.7 Analysis of RA and AF Distribution

The distribution of RA-AF values is an effective method to detect and classify the fracture pattern of concrete and rock materials. Tensile and shear cracks are distinguished using this method by employing values of the AE parameters RA and AF. The formulas are expressed in the RA and AF values as Eqs. 4 and 5.

$$RA \text{ value} = \text{rise time}/\text{maximum amplitude} \quad (4)$$

$$AF \text{ value} = \text{AE counts}/\text{duration} \quad (5)$$

To explore the influence of fracture and failure process during uniaxial cyclic different loading and unloading rate on AE characteristics were compared. The AF-RA distribution of granite obtained from different cyclic loading, i.e., 0.5, 1.5, and 2.5kN/s, is shown in Fig. 10a–c, respectively. The dotted black line in each picture was used as a dividing line to approximate partition the tensile crack zone and shear crack zone. Due to the larger number of RA-AF points with similar values, the superposition and intersection of many RA-AF points would occur in the coordinates, which leads to a drawback in that the characteristics of RA-AF distributions cannot be seen. However, in the first cycle, cracks are not generated. Still, few pre-existing microcracks within the rocks form due to the unloading of granite (intrusive igneous rock) caused by weathering and erosion of overburden. Due to such a low-stress level of the first cycle, the tip of these pre-existing microcracks expands further, causing crack closure. With the increasing cycles, the ratios of tensile cracks decreased, and the ratios of shear cracks increased. This indicated that the proportion of shear cracks is higher; the stress

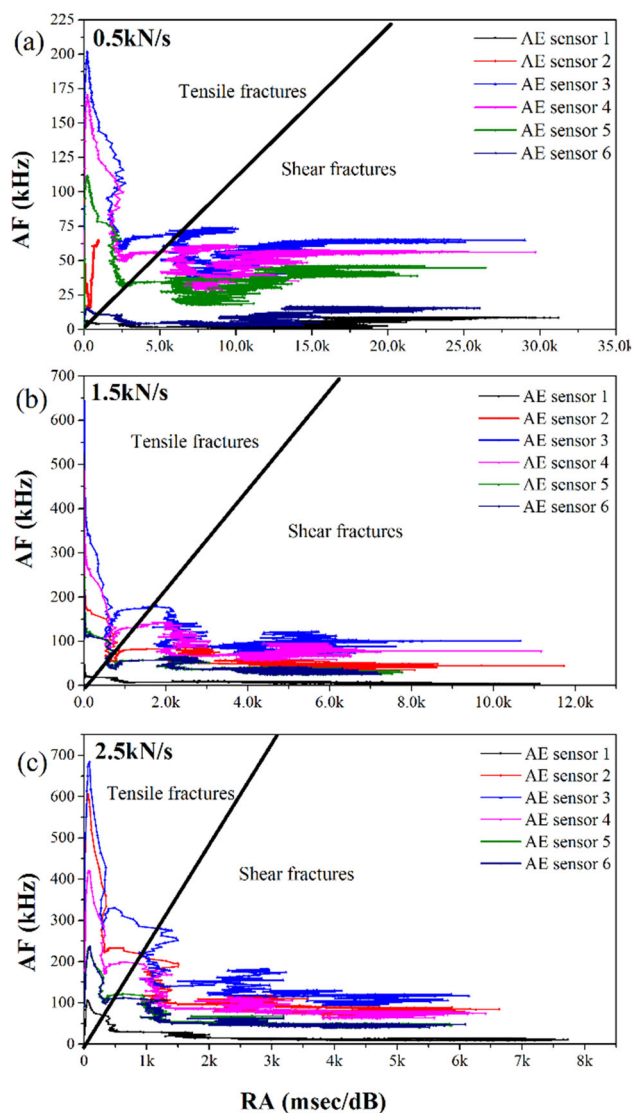


**Fig. 10** Crack classification by the distribution of RA-AF values during different loading–unloading rates at six different AE sensors locations **a** 0.5kN/s **b** 1.5kN/s **c** 2.5kN/s

level is between 30.57 and 60.65%. When the loading rate for 1.5kN/s and 2.5kN/s, in the first cycle the cracks in the rock samples gradually closed, which led to the occurrence of high RA and low AF. Shear stress at this time had a significant impact on the rock samples. Then, during the second to fourth loading–unloading cycles, high AF and low RA emerged. Tensile stress was most likely the primary stress during this time, and numerous microcracks appeared. The internal damage of the rock specimens steadily increases due to the microcracks merging with one another. Simultaneously, the RA value also trended upward as the stress level increased. When the macroscopic failure occurred, the RA and AF values were raised to their maximum, and visible cracks appeared under the combined influence of tensile and shear stress.



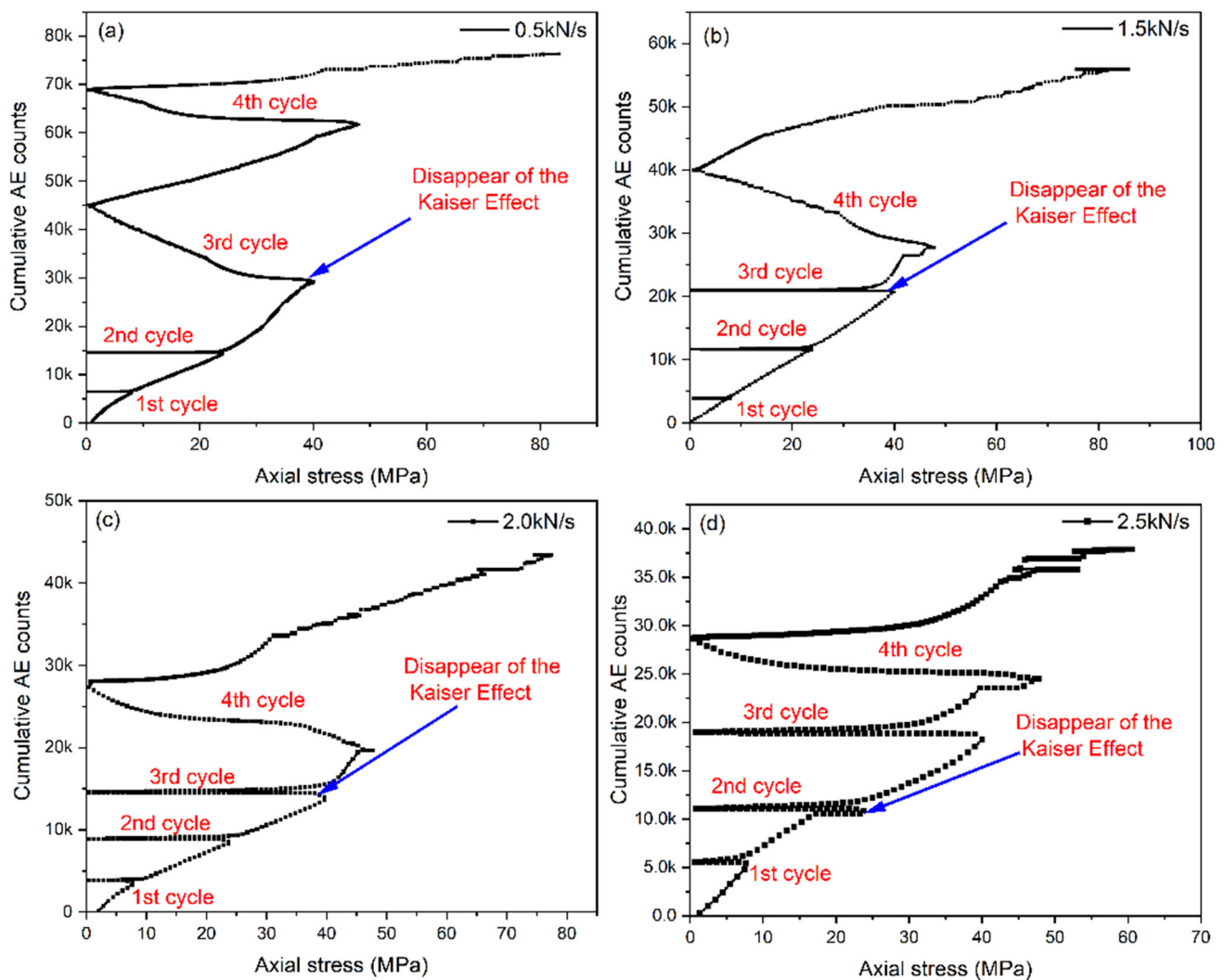
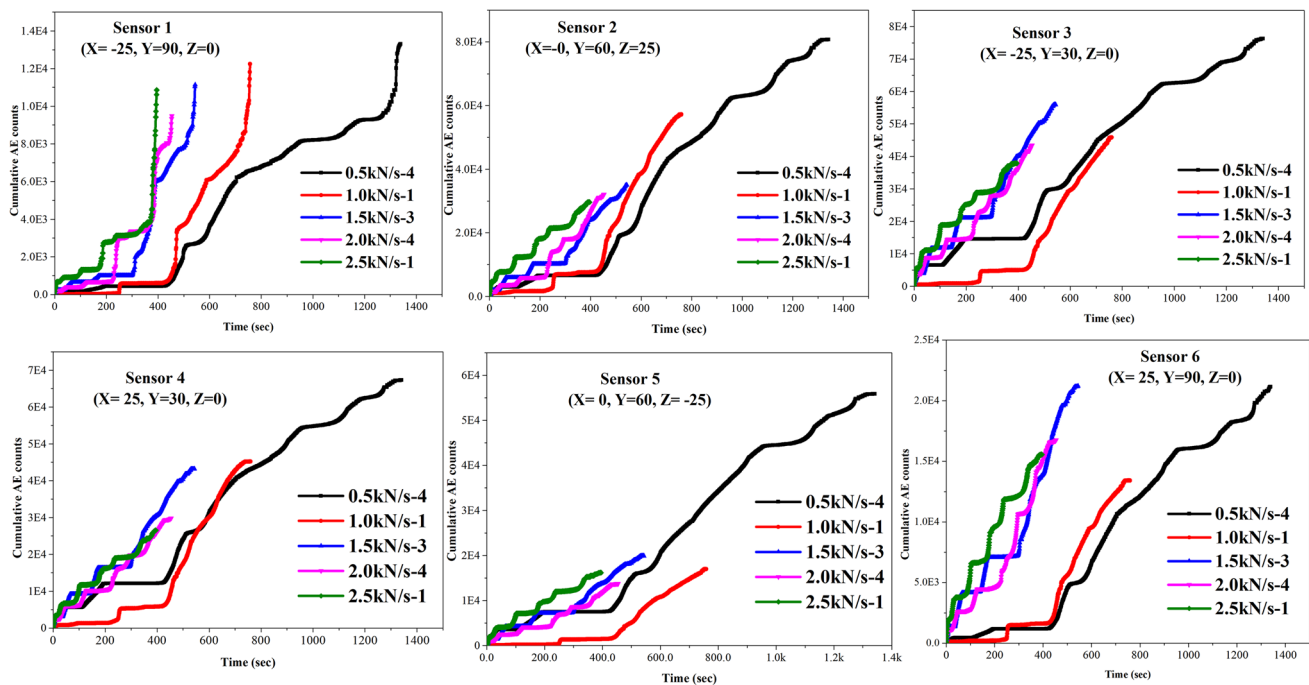


Fig. 11 Accumulative AE counts vs. stress a 0.5 kN/s b 1.5kN/s. c 2.0kN/s d 2.5 kN/s

### 4 Discussions

The granite rock specimen was experimentally investigated from uniaxially cyclic loaded and unloaded four times before it failed. Compared to the earlier cycle, the stress path in the subsequent loading–unloading cycles differs because the induced stress path at the discontinuity associated with (crack closure, crack initiation, crack propagation, and grain boundary) can develop damage accumulation. The AE counts of the entire experimental procedure are plotted in a cumulative form, as shown in Fig. 11. Notably, we used cumulative (accumulated) for the axis of the AE counts in the graphs. The AE count initially increased progressively and then stayed steady when the load approached the predetermined stress during the third and fourth cycles. The cumulative AE count increased significantly after the reloading stress until the sample failed. Under cyclic loading–unloading rates of 0.5, 1.5, 2.0, and 2.5kN/s, the highest cumulative AE counts of the

specimen were 68.5, 40.3, 28.73, and 27.1 k, respectively. This result showed that the 2.5kN/s loading rate caused more severe damage to the internal structure of the granite. Thus, the brittle failure also progressively appears as the cycle duration and loading rates increase. The consolidation may return to its initial state after reloading, indicating that the crack closure and elasticity phases will not be identified as the AE event. Still, the AE phenomenon will differ each time rock material is loaded and unloaded. In various cycles, when the loading is increased, the AE phenomenon will be more noticeable; when the loading is decreased, it will be less so. Therefore, high loading rates severely constrained the rock’s AE activities. In contrast, elastic deformation is the primary deformation state of rock material with low loading rates. Hence, crack initiation and stable growth of fractures become the primary deformation and failure state as the loading–unloading cycle increases. At the unstable crack propagation



**Fig. 12** Variation between accumulated AE counts number and monitoring time of granite

stage, the Felicity effect appears, and the Kaiser effect eventually disappears [61, 62]. Therefore, according to our results, during 0.5, 1.5, and 2.0kN/s cyclic loading, the Kaiser effect disappeared after the third cycle, as shown in Fig. 11a, b, and c. But during 2.5kN/s loading, the Kaiser effect disappeared in the second cycle, as shown in Fig. 11d. This is due to the granite rock being a representative that experienced severe damage below 2.0kN/s cyclic loading. While a typical brittleness enhancement is obtained at 2.5kN/s cyclic loading.

The cumulative AE counts number versus monitoring time under different loading–unloading rates at six different AE sensor locations for all specimens is shown in Fig. 12. The accumulated AE count numbers of the rock specimen show nonlinear gradient growth. From this criterion, it is discovered that the previous maximum stress of 61.12, 60.63, 60.66, and 59.90 MPa at the fourth cycle, when the specimens were held for 948, 332, 251, and 190 secs, respectively, under various cyclic loading rates of 0.5, 1.5, 2.0, and 2.5kN/s.

The counter-Kaiser effect is an additional name for the felicity effect. This explains why AE activity is more evident when the applied stress exceeds the maximum value in the loading history of the previous cycle. Felicity ratio (FR), which typically depicts the degree of rock damage and structural defects, may be used to quantify the rock damage. Rock damage becomes more severe as the FR decreases. Given that if  $FR \geq 1.0$ , The Kaiser effect is affirmed, and there is little to no damage to the rocks. When  $FR < 1.0$ , the Kaiser effect starts to fade, indicating significantly unstable crack propagation forced damage. The Felicity ratio can therefore

be used to determine the magnitude of the Kaiser effect. The Felicity ratio (FR) is the ratio of the stress magnitude of the Kaiser effect ( $\sigma_{AE}$ ) and the highest stress in the previous maximum stress level ( $\sigma_m$ ).

The equation that defines (FR) is Eq. 6:

$$FR = \frac{\sigma_{AE}}{\sigma_m} \quad (6)$$

The maximum stress ( $\sigma_m$ ) and Kaiser effect ( $\sigma_{AE}$ ) for each loading–unloading cycle for all specimens are listed in Table 4. The variation of the FR during increased cycles under different uniaxial cycles loading–unloading rates conditions is illustrated in Fig. 13. As loading–unloading rates are raised, the FR of the rock specimens gradually drops. The FR can be categorized into 4 phases: Phases I, II, III, and IV.

In Phase I, the Felicity ratio is higher than 1.0 ( $FR \geq 1$ ). The pre-existing microcrack in the rock closes under low-stress compaction, which causes the generation of AEs during 0.5, 1.0, 1.5, and 2.0kN/s cyclic loading. Since the rock is not severely damaged during this stage, the AE defects point is primarily caused by the closing of the initial microcracks. The specimen is still in the compaction stage during the first loading–unloading cycles, and as a result, there is not too much of an increase in the number of AEs produced. As a result, the fact that the Felicity effect remains unchanged implies that the Kaiser effect is still present in the crack closure to the linear elastic stage; this demonstrates that the “stress memory” function of the granite rock material is good.

**Table 4** Peak stresses and Kaiser effect stresses for each loading–unloading cycle for rock specimens

	Cycles	$\sigma_m$	$\sigma_{AE1}$	$\sigma_{AE2}$	$\sigma_{AE3}$	$\sigma_{AE4}$	$\sigma_{AE5}$	$\sigma_{AE6}$	FR <sub>1</sub>	FR <sub>2</sub>	FR <sub>3</sub>	FR <sub>4</sub>	FR <sub>5</sub>	FR <sub>6</sub>
0.5kN/s	1	10.00	12.07	11.96	11.53	11.29	10.96	10.53	1.20	1.19	1.15	1.12	1.09	1.05
	2	30.00	31.96	32.03	31.96	31.57	31.44	30.87	1.06	1.06	1.06	1.05	1.04	1.02
	3	50.00	38.46	39.01	36.91	35.04	34.92	33.92	0.76	0.78	0.73	0.70	0.69	0.67
	4	65.00	54.67	50	48.73	44.92	43.12	41.37	0.84	0.76	0.74	0.69	0.66	0.63
1.0kN/s	1	10.00	11.03	10.96	10.58	10.39	10.29	10.12	1.10	1.096	1.05	1.039	1.029	1.012
	2	30.00	28.57	28.93	30.03	29.86	28.57	27.98	0.95	0.96	1.00	0.99	0.95	0.93
	3	48.56	39.12	37.71	38.37	37.43	34.12	39.93	0.80	0.77	0.79	0.77	0.70	0.82
	4	58.96	16.12	21.42	26.51	22.31	19.97	15.01	0.27	0.36	0.44	0.37	0.33	0.25
1.5kN/s	1	10.00	10.23	10.31	10.5	10.56	10.01	10.07	1.02	1.03	1.05	1.05	1.00	1.00
	2	32.96	29.12	28.67	24.73	23.12	28.12	29.12	0.88	0.86	0.75	0.70	0.88	0.88
	3	52.91	46.72	45.92	44.69	46.01	49.01	48.01	0.88	0.86	0.84	0.86	0.90	0.90
	4	63.17	21.96	19.12	20.1	20.01	15.59	14.59	0.34	0.30	0.31	0.31	0.23	0.23
2.0kN/s	1	10.00	9.96	9.93	9.98	9.94	9.99	9.95	0.99	0.99	0.99	0.99	0.99	0.99
	2	30.00	29.01	29.89	28.01	28.67	28.56	15.39	0.96	0.99	0.93	0.95	0.51	0.51
	3	50.00	41.23	47.01	48.21	40.96	38.46	17.12	0.82	0.94	0.96	0.81	0.34	0.34
	4	60.00	16.56	17.29	18.57	10.98	12.96	12.12	0.27	0.28	0.30	0.18	0.20	0.20
2.5kN/s	1	10.00	8.91	8.87	8.57	7.96	7.32	7.57	0.89	0.88	0.85	0.796	0.757	0.75
	2	30.00	21.09	22.01	20.69	20.12	21.59	20.39	0.70	0.73	0.68	0.67	0.67	0.67
	3	50.00	33.57	30.99	32.67	30.43	36.53	33.12	0.67	0.61	0.65	0.60	0.66	0.66
	4	60.00	15.93	10.01	10.59	14.51	11.51	11.43	0.26	0.16	0.17	0.24	0.19	0.19

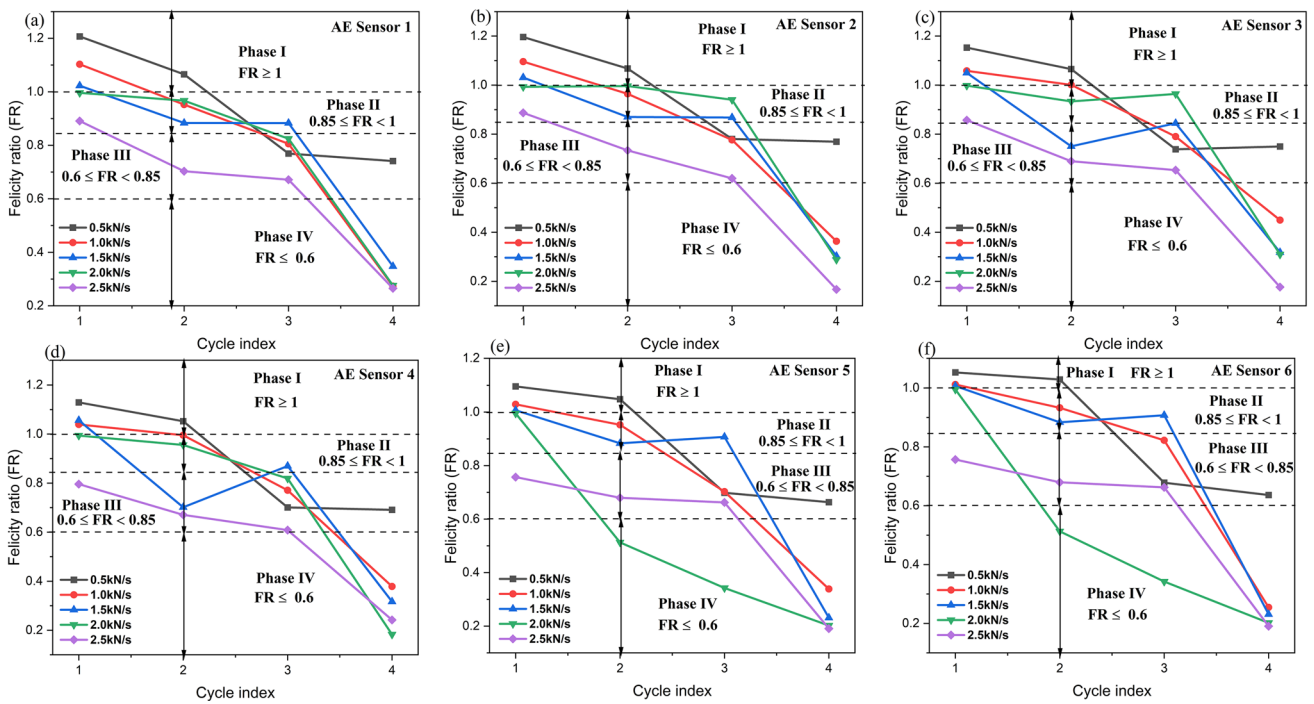


**Fig. 13** Variations in the Felicity ratio of granite rock specimens

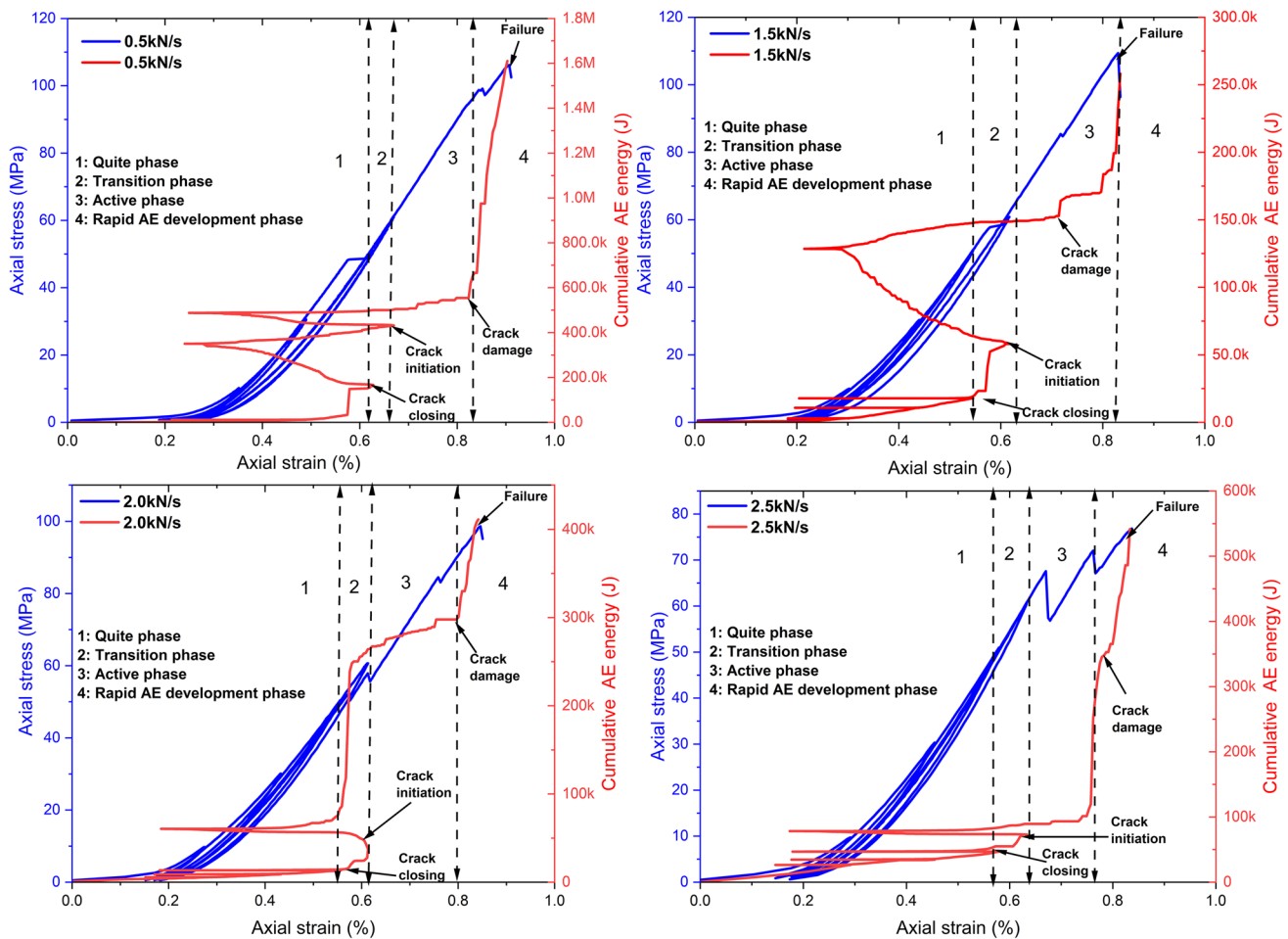


**Fig. 14** Cyclic variation in granite cumulative AE energy with deformation and failure of granite

In Phase II ( $0.85 < FR < 1.0$ ), rock deformation gets intensified while the load keeps rising, and the AE events are active [15, 18, 21, 49]. The coalescence of microcracks and stable crack propagation emerge in this phase, and once the stress surpasses the elastic yield strength of the rock specimens, FR starts to appear.

In Phase III ( $0.6 < FR < 0.85$ ), the ratio then progressively reduces to a value of about one in the intermediate cycles (third cycle), but it then continues to deteriorate, reaching a low point of less than 0.6 in the fourth cycle. In this phase, rock damage continues to accumulate because rock deformation cannot fully recover. The irreversibility of structural deformation becomes apparent at the high-stress stage, resulting in poor stress memory. This phenomenon is linked to the residual strain increases that are characterized by a significant rise in AE events [18, 21]. Therefore, as the FR is decreased, the Kaiser effect disappears, indicating that the rock damage becomes higher due to unstable crack expansion.

In Phase IV ( $FR < 0.6$ ), the rock has reached the point of failure as the stress has escalated. The FR drops under 0.6

as the cracks continue to spread and widen. This decrease indicates that the specimens' crack propagation has been accelerated, and the rock is now on the verge of collapse. Overall, changes in FR for the specimen are like those in other granite specimens tested in the fourth cycle. This may be due to an increase in AE activity that comes earlier and is more intense during this phase [63–68]. Stresses may have been focused around the microcracks after the fourth loading–unloading cycle, leading to many AEs when the rock nearly fractured. As a result, this generates macrocracks, which enhance the instability to induce the failure of granite rock specimens. The evolution of granite's AE energy characteristics throughout an entire cyclic loading test is illustrated in Fig. 14. The AE energy parameters grow nonlinearly during the various rock deformation stages of crack closing, crack initiation, and crack damage. At the failure point, the AE energy reaches its peak before rising sharply. The sharp rise in AE was caused by the energy that is instantly released due to the structural failure of rocks. There is a limit to how much elastic energy can be retained; hence the elastic energy release is the primary cause of rock failure [69, 70].

## 5 Conclusion

In this study, the strength, deformation, failure, and acoustical analysis of granite specimens were conducted by applying varied cyclic loading–unloading rates (0.5, 1.0, 1.5, 2.0, and 2.5kN/s). The verifications of the Kaiser and Felicity effects based on AE parameters were also investigated. The following conclusions were drawn considering the experimental findings:

- (1) The Kaiser effect is observed in the linear elastic stage of granite specimens during below 1.5 kN/s cyclic loading rates. This is shown by microcracks that are in equilibrium during the first and second cycles, suggesting the stress memory function of granite rock masses. But after 2.0kN/s cyclic loading rates, the Kaiser effect was only noticed during the first cycle and disappeared during the second cycle onwards.
- (2) During the unloading phases as the loading–unloading cycles increase, the hysteresis loop continually moves toward the direction of strain increases. As a result, deformation and failure increase with time, and the hysteresis loop gets severe with more cycles and higher loading rates.
- (3) The FR is greater than one for cyclic loading rates of 0.5 and 1.0 kN/s (the first and second cycles). In the subsequent intermediate cycles (the second and third cycles) under 1.5kN/s cyclic loading rates, the FR steadily drops to about 0.8. However, FR decreases even further, reaching less than 0.6 during the fourth cycle for cyclic loading rates of 2.0 and 2.5 kN/s.
- (4) The degree of damage to the rock specimen during the previous cycle can be inferred using the change in FR. Damage from any cycle can only be seen in the next cycle; this is related to the qualitative and quantitative damage measurement of rocks, indicating the extent to which the rock can be safely loaded.

**Acknowledgements** This work was supported by the Institute Post-doctoral Fellowship Program, which was given to the first author (PK Gautam) by the State Key Laboratory of Geohazard Prevention and Geo-environmental Protection, Chengdu University of Technology, Chengdu, China.

## Declarations

**Conflict of interest** The authors declare that they have no conflict of interest exists in the submission of this manuscript.

## References

1. Peng, K.; Zhou, J.; Zou, Q.; Yan, F.: Deformation characteristics of sandstones during cyclic loading and unloading with varying lower

- limits of stress under different confining pressures. *Int. J. Fat.* **127**, 82–100 (2019)
2. Kang, P.; Jiaqi, Z.; Quanle, Z.; Junhui, M.: Fatigue deformation characteristics and damage model of sandstones subjected to cyclic loading: Implications for fatigue life prediction. *Int. J. Geomech.* **22**, 4021261 (2022)
3. Feng, X.-T.; Xu, H.; Yang, C.; Zhang, X.; Gao, Y.: Influence of loading and unloading stress paths on the deformation and failure features of Jinping marble under true triaxial compression. *Rock Mech. Rock Eng.* **53**, 3287–3301 (2020)
4. Feng, F.; Chen, S.; Wang, Y.; Huang, W.; Han, Z.: Cracking mechanism and strength criteria evaluation of granite affected by intermediate principal stresses subjected to unloading stress state. *Int. J. Rock Mech. Min. Sci.* **143**, 104783 (2021)
5. Feng, Q.; Jin, J.; Zhang, S.; Liu, W.; Yang, X.; Li, W.: Study on a damage model and uniaxial compression simulation method of frozen–thawed rock. *Rock Mech. Rock Eng.* **55**, 187–215 (2022)
6. Chen, Y.; Guo, W.; Zuo, J.; Heng, S.; Dou, R.: Effect of triaxial loading and unloading on crack propagation and damage behaviors of sandstone: an experimental study. *Rock Mech. Rock Eng.* **54**, 6077–6090 (2021)
7. Rudajev, V.; Vilhelm, J.; Lokajicek, T.: Laboratory studies of acoustic emission prior to uniaxial compressive rock failure. *Int. J. Rock Mech. Min. Sci.* **37**, 699–704 (2000)
8. Lavrov, A.: The Kaiser effect in rocks: principles and stress estimation techniques. *Int. J. Rock Mech. Min. Sci.* **40**, 151–171 (2003)
9. Benson, P.M.; Thompson, B.D.; Meredith, P.G.; Vinciguerra, S.; Young, R.P.: Imaging slow failure in triaxially deformed Etna basalt using 3D acoustic-emission location and X-ray computed tomography. *Geophys. Res. Letters.* **34**, 456 (2007). <https://doi.org/10.1029/2006GL028721>
10. Zhang, M.; Shimada, H.; Sasaoka, T.; Matsui, K.; Dou, L.: Seismic energy distribution and hazard assessment in underground coal mines using statistical energy analysis. *Int. J. Rock Mech. Min. Sci.* **64**, 192–200 (2013)
11. Tensi, H.M.: The Kaiser-effect and its scientific background. *J. of Acoust. Emission.* **22**, s1–s16 (2004)
12. Goodman, R.E.: Subaudible noise during compression of rocks. *Geol. Soc. Am. Bull.* **74**, 487–490 (1963)
13. Kurita, K.; Fujii, N.: Stress memory of crystalline rocks in acoustic emission. *Geophys. Res. Lett.* **6**, 9–12 (1979)
14. Li, Y.; Schmitt, D.R.: Effects of Poisson’s ratio and core stub length on bottomhole stress concentrations. *Int. J. Rock Mech. Min. Sci.* **34**, 761–773 (1997)
15. Lavrov, A.: Kaiser effect observation in brittle rock cyclically loaded with different loading rates. *Mech. Mater.* **33**, 669–677 (2001)
16. Zhao, X.: Application of the Kaiser effect of acoustic emission to measure vertical stress in an underground mine. *Insight-Non-destructive Test. Cond. Monit.* **54**, 662–666 (2012)
17. Holcomb, D.J.; Costin, L.S.: Detecting damage surfaces in brittle materials using acoustic emissions. *J. Appl. Mech.* **53**(3), 536–544 (1986). <https://doi.org/10.1115/1.3171807>
18. Rao, M.; Ramana, Y.V.: A study of progressive failure of rock under cyclic loading by ultrasonic and AE monitoring techniques. *Rock Mech. Rock Eng.* **25**, 237–251 (1992)
19. Cox, S.J.D.; Meredith, P.G.: Microcrack formation and material softening in rock measured by monitoring acoustic emissions. *Int J Rock Mech Min. Sci. Geomech. Abst.* **30**, 11–24 (1993)
20. Lockner, D.: The role of acoustic emission in the study of rock fracture. *Int. J. Rock Mech. Min. Sci.* **30**, 883–899 (1993). [https://doi.org/10.1016/0148-9062\(93\)90041-B](https://doi.org/10.1016/0148-9062(93)90041-B)
21. Li, C.; Nordlund, E.: Assessment of damage in rock using the Kaiser effect of acoustic emission. *Int. J. Rock Mech. Min. Sci. Geomech. Abst.* **30**, 943–946 (1993)



22. Li, C.; Nordlund, E.: Experimental verification of the Kaiser effect in rocks. *Rock Mech. Rock Eng.* **26**, 333–351 (1993)
23. Pestman, B.J.; Van Munster, J.G.: An acoustic emission study of damage development and stress-memory effects in sandstone. *Int. J. Rock Mech. Min. Sci. Geomech. Abstr.* **33**, 585–593 (1996)
24. Dai, S.T.; Labuz, J.F.: Damage and failure analysis of brittle materials by acoustic emission. *J. Mater. Civ. Eng.* **9**, 200–205 (1997)
25. Akesson, U.; Hansson, J.; Stigh, J.: Characterisation of microcracks in the Bohus granite, western Sweden, caused by uniaxial cyclic loading. *Eng. Geol.* **72**, 131–142 (2004)
26. Tham, L.G.; Liu, H.; Tang, C.A.; Lee, P.K.K.; Tsui, Y.: On tension failure of 2-D rock specimens and associated acoustic emission. *Rock Mech. Rock Eng.* **38**, 1–19 (2005)
27. Ganne, P.; Vervoort, A.; Wevers, M.: Quantification of pre-peak brittle damage: correlation between acoustic emission and observed micro-fracturing. *Int. J. Rock Mech. Min. Sci.* **44**, 720–729 (2007)
28. Ishida, T.; Kanagawa, T.; Kanaori, Y.: Source distribution of acoustic emissions during an in-situ direct shear test: Implications for an analog model of seismogenic faulting in an inhomogeneous rock mass. *Eng. Geol.* **110**, 66–76 (2010)
29. Spasova, L.M.; Ojovan, M.I.; Gibb, F.G.F.: Acoustic emission on melting/solidification of natural granite simulating very deep waste disposal. *Nucl. Eng. Des.* **248**, 329–339 (2012)
30. Yang, S.-Q.; Jing, H.-W.; Wang, S.-Y.: Experimental investigation on the strength, deformability, failure behavior and acoustic emission locations of red sandstone under triaxial compression. *Rock Mech. Rock Eng.* **45**, 583–606 (2012)
31. Zhao, X.G.; Cai, M.; Wang, J.; Ma, L.K.: Damage stress and acoustic emission characteristics of the Beishan granite. *Int. J. Rock Mech. Min. Sci.* **64**, 258–269 (2013)
32. Zhao, X.G.; Wang, J.; Cai, M.; Cheng, C.; Ma, L.K.; Su, R.; Zhao, F.; Li, D.J.: Influence of unloading rate on the strainburst characteristics of Beishan granite under true-triaxial unloading conditions. *Rock Mech. Rock Eng.* **47**, 467–483 (2014)
33. Momeni, A.; Karakus, M.; Khanlari, G.R.; Heidari, M.: Effects of cyclic loading on the mechanical properties of a granite. *Int. J. Rock Mech. Min. Sci.* **77**, 89–96 (2015)
34. Fu, X.; Xie, Q.; Liang, L.: Comparison of the Kaiser effect in marble under tensile stresses between the Brazilian and bending tests. *Bull. Eng. Geol. Env.* **74**, 535–543 (2015)
35. Meng, Q.; Zhang, M.; Han, L.; Pu, H.; Nie, T.: Effects of acoustic emission and energy evolution of rock specimens under the uniaxial cyclic loading and unloading compression. *Rock Mech. Rock Eng.* **49**, 3873–3886 (2016)
36. Ranjith, P.G.; Fourar, M.; Pong, S.F.; Chian, W.; Haque, A.: Characterisation of fractured rocks under uniaxial loading states. *Int. J. Rock Mech. Min. Sci.* **41**, 43–48 (2004)
37. Liu, B.; Ma, Y.; Zhang, G.; Xu, W.: Acoustic emission investigation of hydraulic and mechanical characteristics of muddy sandstone experienced one freeze-thaw cycle. *Cold Reg. Sci. Technol.* **151**, 335–344 (2018)
38. Wu, J.; Feng, M.; Yu, B.; Han, G.: The length of pre-existing fissures effects on the mechanical properties of cracked red sandstone and strength design in engineering. *Ultrasonics* **82**, 188–199 (2018)
39. Huang, Y.-H.; Yang, S.-Q.; Hall, M.R.; Zhang, Y.-C.: The effects of NaCl concentration and confining pressure on mechanical and acoustic behaviors of brine-saturated sandstone. *Energies* **11**, 385 (2018)
40. Zhou, T.; Han, Z.; Li, D.; Chen, J.: Experimental study of the mechanical and fracture behavior of flawed sandstone subjected to coupled static-repetitive impact loading. *Theoret. Appl. Fract. Mech.* **117**, 103161 (2022)
41. B5706, J.-I.: Monitoring method for active cracks in concrete by acoustic emission. Federation of Construction Material Industries, Japan. 23–28 (2003)
42. Lou, Y.; Zhang, G.; Wang, X.: Study on fracture mechanism of hydraulic fracturing in sandstone by acoustic emission parameters. *Proc. Eng.* **191**, 291–298 (2017). <https://doi.org/10.1016/j.proeng.2017.05.184>
43. Heap, M.J.; Vinciguerra, S.; Meredith, P.G.: The evolution of elastic moduli with increasing crack damage during cyclic stressing of a basalt from Mt. Etna volcano. *Tectonophys.* **471**, 153–160 (2009)
44. Ma, L.; Liu, X.; Wang, M.; Xu, H.; Hua, R.; Fan, P.; Jiang, S.; Wang, G.; Yi, Q.: Experimental investigation of the mechanical properties of rock salt under triaxial cyclic loading. *Int. J. Rock Mech. Min. Sci.* **62**, 34–41 (2013)
45. Wang, Z.; Li, S.; Qiao, L.; Zhao, J.: Fatigue behavior of granite subjected to cyclic loading under triaxial compression condition. *Rock Mech. Rock Eng.* **46**, 1603–1615 (2013)
46. Martin, C.D.; Chandler, N.A.: The progressive fracture of Lac du Bonnet granite. In: *International journal of rock mechanics and mining sciences and geomechanics abstracts*, pp. 643–659. Elsevier, UK (1994)
47. Yang, S.-Q.; Ranjith, P.G.; Huang, Y.-H.; Yin, P.-F.; Jing, H.-W.; Gui, Y.-L.; Yu, Q.-L.: Experimental investigation on mechanical characteristics of sandstone under triaxial cyclic loading. *Geophys. J. Int.* **201**, 662–682 (2015)
48. Liu, Y.; Dai, F.: A review of experimental and theoretical research on the deformation and failure behavior of rocks subjected to cyclic loading. *J. Rock Mech. Geotechn. Eng.* **13**, 1203–1230 (2021)
49. Meng, Q.; Zhang, M.; Han, L.; Pu, H.; Chen, Y.: Acoustic emission characteristics of red sandstone specimens under uniaxial cyclic loading and unloading compression. *Rock Mech. Rock Eng.* **51**, 969–988 (2018)
50. Miao, S.; Xia, D.; Yang, P.; Liang, M.: Acoustic emission and damage characteristics of granite under graded cyclic loading. *Arab. J. Geosci.* **15**, 977 (2022)
51. Xiao, J.-Q.; Ding, D.-X.; Jiang, F.-L.; Xu, G.: Fatigue damage variable and evolution of rock subjected to cyclic loading. *Int. J. Rock Mech. Min. Sci.* **47**, 461–468 (2010)
52. Qiu, S.-L.; Feng, X.-T.; Xiao, J.-Q.; Zhang, C.-Q.: An experimental study on the pre-peak unloading damage evolution of marble. *Rock Mech. Rock Eng.* **47**, 401–419 (2014)
53. Fuenkajorn, K.; Phueakphum, D.: Effects of cyclic loading on mechanical properties of Maha Sarakham salt. *Eng. Geol.* **112**, 43–52 (2010)
54. Eberhardt, E.; Stead, D.; Stimpson, B.: Quantifying progressive pre-peak brittle fracture damage in rock during uniaxial compression. *Int. J. Rock Mech. Min. Sci.* **36**, 361–380 (1999)
55. Erarslan, N.; Williams, D.J.: Investigating the effect of cyclic loading on the indirect tensile strength of rocks. *Rock Mech. Rock Eng.* **45**, 327–340 (2012)
56. Tatsuoka, F.; Lo Presti, D.; Kohata, Y.: Deformation characteristics of soils and soft rocks under monotonic and cyclic loads and their relationships. (1995)
57. Jiang, C.; Lu, T.; Zhang, D.; Li, G.; Duan, M.; Chen, Y.; Liu, C.: An experimental study of deformation and fracture characteristics of shale with pore-water pressure and under triaxial cyclic loading. *Royal Soc. Open Sci.* **5**, 180670 (2018)
58. Meng, Q.; Liu, J.-F.; Ren, L.; Pu, H.; Chen, Y.: Experimental study on rock strength and deformation characteristics under triaxial cyclic loading and unloading conditions. *Rock Mech. Rock Eng.* **54**, 777–797 (2021)
59. Zhang, G.; Li, H.; Wang, M.; Li, X.; Wang, Z.; Deng, S.: Crack-induced acoustic emission and anisotropy variation of brittle rocks containing natural fractures. *J. Geophys. Eng.* **16**, 599–610 (2019)
60. Beno Gutenberg, C.R.: *Seismicity of the earth and associated phenomena*. Princeton University Press, Princeton (1954)
61. Zhang, M.; Meng, Q.; Liu, S.: Energy evolution characteristics and distribution laws of rock materials under triaxial cyclic loading and unloading compression. *Adv. Mater. Sci. Eng.* **2017**, 1–16 (2017)

62. Chen, Y.; Irfan, M.; Song, C.: Verification of the Kaiser effect in rocks under tensile stress: experiment using the Brazilian test. *Int. J. Geomech.* **18**, 4018059 (2018)
63. Zhang, Y.; Chen, Y.; Yu, R.; Hu, L.; Irfan, M.: Effect of loading rate on the felicity effect of three rock types. *Rock Mech. Rock Eng.* **50**, 1673–1681 (2017)
64. Liu, Y.I.; Dai, F.; Xu, N.; Zhao, T.; Feng, P.: Experimental and numerical investigation on the tensile fatigue properties of rocks using the cyclic flattened Brazilian disc method. *Soil Dyn. Earthq. Eng.* **105**, 68–82 (2018)
65. Liu, Y.; Dai, F.; Fan, P.; Xu, N.; Dong, L.: Experimental investigation of the influence of joint geometric configurations on the mechanical properties of intermittent jointed rock models under cyclic uniaxial compression. *Rock Mech. Rock Eng.* **50**, 1453–1471 (2017)
66. Liu, Y.; Dai, F.: A damage constitutive model for intermittent jointed rocks under cyclic uniaxial compression. *Int. J. Rock Mech. Min. Sci.* **103**, 289–301 (2018)
67. Bagde, M.N.; Petroš, V.: The effect of machine behaviour and mechanical properties of intact sandstone under static and dynamic uniaxial cyclic loading. *Rock Mech. Rock Eng.* **38**, 59–67 (2005)
68. Bagde, M.N.; Petroš, V.: Fatigue and dynamic energy behaviour of rock subjected to cyclical loading. *Int. J. Rock Mech. Min. Sci.* **46**, 200–209 (2009)
69. Liu, Y.; Dai, F.; Dong, L.; Xu, N.; Feng, P.: Experimental investigation on the fatigue mechanical properties of intermittently jointed rock models under cyclic uniaxial compression with different loading parameters. *Rock Mech. Rock Eng.* **51**, 47–68 (2018)
70. Liu, Y.; Dai, F.; Feng, P.; Xu, N.: Mechanical behavior of intermittent jointed rocks under random cyclic compression with different loading parameters. *Soil Dyn. Earthq. Eng.* **113**, 12–24 (2018)

Springer Nature or its licensor (e.g. a society or other partner) holds exclusive rights to this article under a publishing agreement with the author(s) or other rightsholder(s); author self-archiving of the accepted manuscript version of this article is solely governed by the terms of such publishing agreement and applicable law.

